Construction and Building Materials 449 (2024) 138252

Contents lists available at ScienceDirect

Construction and Building Materials

journal homepage: www.elsevier.com/locate/conbuildmat

# Experimental study of the quasi-static axial compressive resistance of pultruded GFRP composite stub columns

João Alfredo de Lazzari [a,b,*], José Gonilha [a], João R. Correia [a], Nuno Silvestre [b]

[a] CERIS, Instituto Superior Técnico, Universidade de Lisboa, Av. Rovisco Pais 1, Lisboa 1049-001, Portugal
[b] IDMEC, Instituto Superior Técnico, Universidade de Lisboa, Av. Rovisco Pais 1, Lisboa 1049-001, Portugal

ARTICLE INFO

*Keywords:*
Pultruded profiles
Crushing
Delamination
Axially compressed members
Experimental tests
Design guidelines

ABSTRACT

This paper presents an experimental investigation on the crushing behaviour of full-section pultruded glass fibre reinforced polymer (pGFRP) profiles with 11 different cross-section geometries, encompassing 6 different shapes (C, I, W, SHS, RHS, L sections). Quasi-static axial compressive tests were conducted on stub column specimens, mitigating second-order and buckling effects. The crushing phenomenon of the pGFRP profiles was investigated regarding the following aspects: (i) influence of end surface flatness, (ii) analysis of load/stress *vs.* strain behaviour, (iii) definition of relative slenderness thresholds to avoid buckling, (iv) determination of full-section compressive strength for various cross-sections, and (v) correlation of geometrical and mechanical experimental data. The results show that when the relative slenderness was limited to 0.7, no buckling occurred, and the load was uniformly applied across the section of the profiles. Additionally, for the different cross-section geometries, the estimates of resistance to crushing of pGFRP stub columns obtained from compressive coupon tests were non-conservative: in average, the resistance to crushing of full-section stub columns was around 60 % of those estimates. Unlike the coupon tests, the stub columns presented complex failure with multiple damage modes, which were attributed to the non-uniformity of material properties across the section walls. The correlation analysis provided insights into the linear dependency of the full-section compressive strength with geometrical and material properties. Surprisingly, shear strengths were shown to play a more relevant role in the crushing phenomenon of stub columns than compressive strength. The findings of this study will contribute to the drafting of improved design guidelines able to estimate more accurately (and likely more reliably) the compressive resistance to crushing.

## 1. Introduction

Pultruded glass-fibre reinforced polymer (pGFRP) profiles are becoming more popular in the construction industry, where they are now seen as a viable option for lightweight structures, offering high strength and durability [1,2]. However, due to the relatively recent structural use of pGFRP profiles, there are still gaps in the knowledge of their mechanical behaviour and structural response. A critical area that warrants considerable attention is the structural behaviour of pGFRP profiles under compressive loads.

In general, for composites subjected to compressive loads, the fibres parallel to the load direction are likely to bear most of the load. Nevertheless, the polymeric matrix plays a vital role: besides guaranteeing the load distribution among the fibres, it provides them with lateral restraint, thus preventing fibre buckling. This lateral restraint tends to generate an untrivial strain field in the matrix, which exhibits predominantly shear or extensional strains [3–5]. Owing to these strain fields, compressive fracture may occur at stress levels lower than those observed in tension [3], underscoring the importance of duly considering compressive failure in design guidelines of fibre reinforced polymer (FRP) structures [6–10].

In what concerns the failure mechanisms of FRP laminates, Rosen [3] presented pioneering research for composites used in aerospace applications. Later, in 1997, a comprehensive review by Fleck [11] provided further insights, identifying various failure modes of FRP composites subjected to compressive loading along the fibre direction, namely: (i) elastic micro-buckling, (ii) plastic micro-buckling (kink band), (iii) fibre crushing, (iv) splitting, (v) buckle-delamination, and (vi) shear band formation [3]. Currently, the standardized test procedures to determine the in-plane compressive strength of composite laminates [12] refer the

* Corresponding author at: CERIS, Instituto Superior Técnico, Universidade de Lisboa, Av. Rovisco Pais 1, Lisboa 1049-001, Portugal.
*E-mail address:* joao.lazzari@tecnico.ulisboa.pt (J.A. Lazzari).

https://doi.org/10.1016/j.conbuildmat.2024.138252
Received 9 April 2024; Received in revised form 2 September 2024; Accepted 5 September 2024
Available online 28 September 2024

following failure modes as "valid": brooming, delamination, through-thickness, kink bands, long-splitting, transverse shear, explosive and multi-mode. Recently, based on a fractographic study, Opelt et al. [13] grouped nine different compression failures modes of composite laminates into the following four failure types: (i) shear, (ii) interlaminar, (iii) interfacial, and (iv) kink-band. This recent study focused on different types of laminated composites tailored for aerospace engineering applications, which present major differences compared to pGFRP profiles used in civil engineering structural applications.

According to the European Technical Specification CEN/TS 19101:2022 [9], the compressive resistance to crushing of pGFRP profiles is estimated considering the in-plane compressive strength in the longitudinal direction ($f_{x,c}$) obtained from standardized tests on small coupons. Even though a recent procedure to determine the full-section compressive strength ($f_{SC}$) of pGFRP profiles has been published (ISO 23930:2023 [14]), such property is often determined by testing laminates extracted from the cross-section's walls according to the combined loading compression (CLC) method (ASTM D6641–14 [12] and EN 14126 [15]). However, recent experimental studies, described ahead, indicate that this approach may greatly overestimate the actual compressive resistance to crushing of full-section pGFRP profiles, especially if they are very stocky [16–20].

Guades et al. [16] conducted coupon tests following ASTM D695 [21], using specimens extracted from the walls of pGFRP profiles with square hollow sections (SHS), and compared those material-level results with those of full-section compression tests. The authors observed that the compressive resistance obtained from full-section tests was approximately 60 % of that derived from coupon tests, but did not provide a specific reason for this discrepancy. Similarly, Al-Saadi et al. [17] conducted a study on pGFRP tubes, where they also noted disparities in axial compression resistance estimates considering coupon tests [21] and full-section test results. The full-section test results were approximately 67 % of the estimate from coupon tests for SHS. The authors attributed this discrepancy to factors such as the plate slenderness ratio and layup configuration, leading to failure by splitting at the corners and crushing at the ends.

Ramos [18] performed an extensive experimental campaign in pGFRP stub columns with several I-sections. The author identified a lower resistance to material crushing in full-section compression tests, around 50 % compared to CLC coupon tests. Four potential factors were identified, including: (i) mechanical property heterogeneity across the cross-section (namely in web-flange junctions), (ii) variations in the compressive strength obtained from different test standards (*e.g.*, from CLC method [12,15] and ASTM D695 [21]), (iii) increased likelihood of defects in full-section tests ("size effects"), and (iv) influence of surface flatness in full-section compression specimens.

Recently, Wu et al. [19] conducted tests on pGFRP channel columns with lengths ranging from 100 mm to 1400 mm. The authors observed significantly lower compressive strength estimates from coupon tests (around 40 % of coupon tests) for stub columns measuring 100 mm and 200 mm in length. They attributed this to (i) irregularities in the cross-section shape, leading to non-uniform stress distribution, (ii) non-uniform fibre distribution caused by the pultrusion process and material imperfections, and (iii) local crushing resulting from stress concentrations or material imperfections, interacting with the local buckling of the flange or web.

Higgoda et al. [20] conducted stub column tests on pGFRP profiles with circular hollow sections (CHS) and compared the results with estimates from coupon tests [21]. In cases where the columns were very stocky (length-to-diameter, $L/D$, equal to 1), their resistance was close to that predicted from the coupon tests (approximately 88 %). However, for stub columns with $L/D = 3$, still considered stocky but buckling-free, there was a 45 % reduction in the full-section compressive resistance compared to that predicted from the coupon tests, with failure occurring at the bottom end due to fibre and matrix crushing. The authors suggested that premature crushing failure is associated to the circular geometry of the tube, aligning with the findings of Al-Saadi et al. [17].

Several other authors, focusing on the behaviour of composite materials under harsh environments, presented additional experimental data on the compressive resistance of full-section pGFRP profiles [22–26]. However, since that was not the main focus of those studies, the methodologies used to select the length of the columns was not always clear, and it is possible that local buckling may have played a part in the failure modes reported. Moreover, most tests were conducted under load control, making it difficult to identify buckling phenomena. Additionally, in most cases, the material properties reported were given by the manufacturer, and not by material characterization tests conducted on the profiles used, therefore precluding the obtention of accurate resistance predictions.

The aim of this study is to experimentally investigate the quasi-static crushing failure of full-section pGFRP profiles, with different cross-sections and produced by different manufacturers. The study includes 11 cross-sections, with 6 different shapes, produced by 3 different manufacturers. The experimental investigation comprises: (i) the mechanical characterization of the composite materials through standardized tests on coupons extracted from the sections' walls, and (ii) testing the corresponding full-section stub columns. A five-stage analysis is carried out including: (i) assessment of the influence of the stub column end surface flatness; (ii) load/stress *vs*. strain behaviour, using digital image correlation (DIC); (iii) definition of relative slenderness limit to avoid buckling; (iv) determination of full-section compressive strength for several cross-sections, and comparison with predictions based on in-plane compressive strength obtained from standardized tests on coupons, and (v) correlation of geometrical and mechanical parameters, from both full-section and coupon test data.

## 2. Experimental programme

### 2.1. Materials

The pGFRP profiles considered in the present study were provided by three different manufacturers and comprised six different cross-sections shapes: channel section, I-section, angle section, square hollow section (SHS), rectangular hollow section (RHS) and wide-flange section [27–29], illustrated in Fig. 1. The main geometrical characteristics of the pGFRP profiles are summarized in Table 1, including the profile label, the cross-section shape, the manufacturer label (associated to the manufacturer description in Table 2), and the nominal dimensions: height ($H_n$), width ($B_n$), thickness ($t_n$), external radius ($R_n$) and internal radius ($r_n$). Table 2 indicates the type of resin, fibre reinforcement, colour, use of UV inhibitor and flame retardant, and commercial designation of each series of profiles used in the tests.

### 2.2. Coupon tests

The mechanical properties of the pGFRP profiles were obtained from standardized tests on small-scale coupons extracted from the walls of the profiles. The mechanical properties of profile CI6 can be found in the work of Almeida-Fernandes et al. [30] (except the Poisson ratio $\nu_{xy,c}$, which was reported by Ramos [18]), and the mechanical properties of profile AI8, which can be found in Gonilha et al. [31] and Ramos [18].

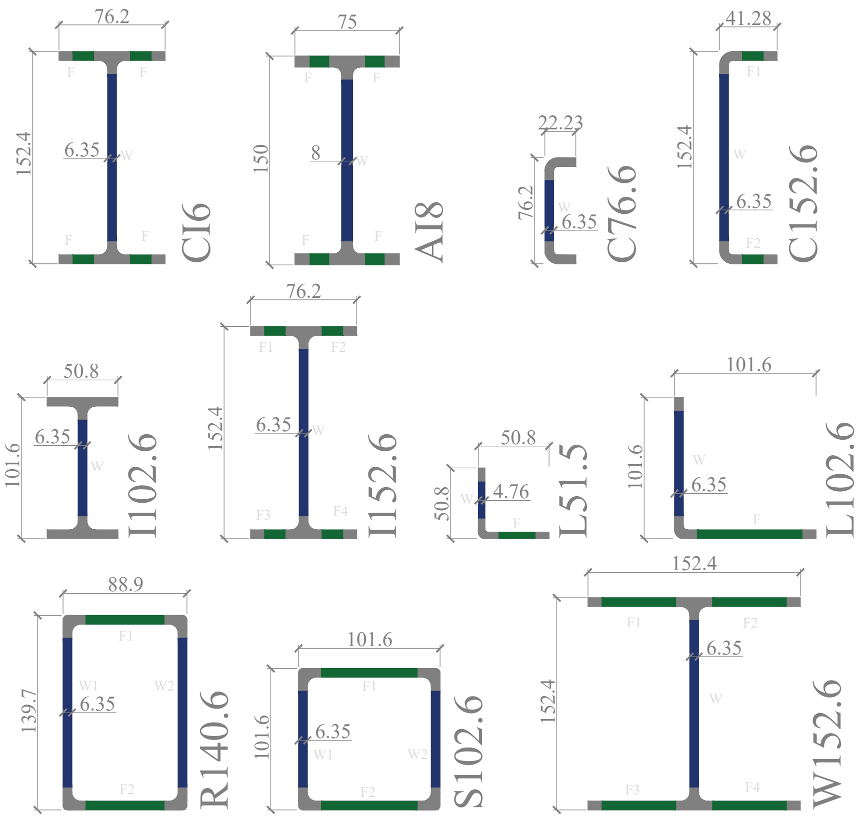


**Fig. 1.** pGFRP profiles nominal geometry and profile label (dimensions in mm). [coloured areas correspond to zones where coupons were extracted from the flange/web/leg].

**Table 1**
Characteristics of pGFRP profiles.

| Profile label | Shape | Manufacturer label | Nominal dimensions (mm) | | | | |
|---|---|---|---|---|---|---|---|
| | | | $H_n$ | $B_n$ | $t_n$ | $R_n$ | $r_n$ |
| CI6 | I-section | CP1 | 152.40 | 76.20 | 6.35 | - | 6.35 |
| AI8 | I-section | AP1 | 150.00 | 75.00 | 8.00 | - | 5.00 |
| C76–6 | C-section | SV1 | 76.20 | 22.23 | 6.35 | 9.53 | 3.18 |
| C152–6 | C-section | SV1 | 152.40 | 41.28 | 6.35 | 9.53 | 3.18 |
| I102–6 | I-section | SV1 | 101.60 | 50.80 | 6.35 | - | 3.18 |
| I152–6 | I-section | SP1 | 152.40 | 76.20 | 6.35 | - | 3.18 |
| L51–5 | L-section | SP2 | 50.80 | 50.80 | 4.76 | 4.76 | 3.18 |
| L102–6 | L-section | SV1 | 101.60 | 101.60 | 6.35 | 6.35 | 3.18 |
| R140–6 | RHS | SP1 | 139.70 | 88.90 | 6.35 | 9.53 | 3.18 |
| S102–6 | SHS | SV1 | 101.60 | 101.60 | 6.35 | 3.96 | 3.18 |
| W152–6 | W-section | SV1 | 152.40 | 152.40 | 6.35 | - | 3.18 |

For the remaining profiles, the properties were determined in the scope of the present experimental campaign. Fig. 1 indicates the zones of the various cross-sections where the coupons were extracted from. For the C76–6 and I102–6 profiles, the coupon specimens were extracted from the web of the profiles only (due to the size limitations of the flange walls).

The coupon tests were conducted in two universal testing machines (UTM), from *Intron*, model 5989 (600 kN capacity) and model 5982 (100 kN capacity), ensuring the setup configuration and load capacity were suitable for various standard procedures and expected maximum loads. A video-extensometer system was employed to determine the relative displacements of various target points marked on the specimens, enabling the assessment of deformations. This system comprises a 10-bit Sony CCD XCLU100 camera connected to a Fujinon F35SA-1 lens with a

**Table 2**
Characteristics of pGFRP profiles supplied by different manufacturers.

| Label | Manufacturer | Resin | Fiber | Colour | UV inhibitor | Flame retardant | Series |
|---|---|---|---|---|---|---|---|
| AP1 | Alto | Polyester | E-glass | White | Yes | No | Standard |
| CP1 | Creative | Polyester | E-glass | Olive Green | Yes | No | Pultex® SuperStructural 1500 |
| SP1 | Strongwell | Polyester | E-glass | Dark Grey | Yes | Yes | EXTREN® 525 |
| SP2 | Strongwell | Polyester | E-glass | Olive Green | Yes | No | EXTREN® 500 |
| SV1 | Strongwell | Vinyl Ester | E-glass | Beige | Yes | Yes | EXTREN® 625 |

**Table 3**
Strength and physical properties obtained from coupon tests extracted from the pGFRP profile walls. [mean values, standard deviation (SD), coefficient of variation (CoV) and number of specimens tested (*n*)].

| Profile label | Statistical Parameter | T-11* | T-22* | C-11* | C-22* | C-22B* | S-12* | S-21* | I-31* | CA* |
|---|---|---|---|---|---|---|---|---|---|---|
| | | $f_{x,t}$ (MPa) | $f_{y,t}$ (MPa) | $f_{x,c}$ (MPa) | $f_{y,c}$ (MPa) | $f_{y,c}$ (MPa) | $f_{xy,v}$ (MPa) | $f_{yx,v}$ (MPa) | $f_{zx,ILS}$ (MPa) | $w$% (%) |
| C76–6 | *Mean* | 408 | - | 561 | - | 185 | 107 | - | 38 | 57 % |
| | *SD* | 9.50 | - | 23.44 | - | 5.03 | 3.36 | - | 0.55 | 0.1 % |
| | *CoV* | 2 % | - | 4 % | - | 3 % | 3 % | - | 1 % | 0 % |
| | *n* | 6 | - | 5 | - | 6 | 6 | - | 6 | 2 |
| C152–6 | *Mean* | 447 | 87 | 564 | 194 | 175 | 113 | 107 | 38 | 60 % |
| | *SD* | 26.10 | 4.15 | 58.25 | 6.84 | 14.25 | 5.26 | 3.17 | 1.69 | 2.9 % |
| | *CoV* | 6 % | 5 % | 10 % | 4 % | 8 % | 5 % | 3 % | 4 % | 5 % |
| | *n* | 13 | 6 | 11 | 6 | 12 | 6 | 6 | 12 | 6 |
| I102–6 | *Mean* | 403 | - | 515 | - | 164 | 114 | - | 37 | 65 % |
| | *SD* | 11.30 | - | 30.79 | - | 6.59 | 4.39 | - | 0.65 | 0.2 % |
| | *CoV* | 3 % | - | 6 % | - | 4 % | 4 % | - | 2 % | 0 % |
| | *n* | 6 | - | 5 | - | 6 | 6 | - | 6 | 2 |
| I152–6 | *Mean* | 504 | 88 | 410 | 133 | 107 | 84 | 93 | 26 | 63 % |
| | *SD* | 114.77 | 3.84 | 51.38 | 11.61 | 16.51 | 6.35 | 1.62 | 1.35 | 6.7 % |
| | *CoV* | 23 % | 4 % | 13 % | 9 % | 15 % | 8 % | 2 % | 5 % | 11 % |
| | *n* | 15 | 6 | 14 | 6 | 14 | 8 | 6 | 14 | 10 |
| L51–5 | *Mean* | 479 | - | 417 | - | 126 | 95 | - | 31 | 55 % |
| | *SD* | 55.12 | - | 40.99 | - | 8.14 | 3.70 | - | 1.47 | 3.7 % |
| | *CoV* | 12 % | - | 10 % | - | 6 % | 4 % | - | 5 % | 7 % |
| | *n* | 6 | - | 6 | - | 6 | 6 | - | 6 | 4 |
| L102–6 | *Mean* | 443 | - | 533 | - | 154 | 104 | - | 40 | 58 % |
| | *SD* | 23.49 | - | 48.37 | - | 14.26 | 3.20 | - | 1.38 | 0.7 % |
| | *CoV* | 5 % | - | 9 % | - | 9 % | 3 % | - | 3 % | 1 % |
| | *n* | 8 | - | 7 | - | 8 | 6 | - | 8 | 4 |
| R140–6 | *Mean* | 542 | 67 | 462 | 137 | 113 | 85 | 81 | 31 | 63 % |
| | *SD* | 71.88 | 5.10 | 52.51 | 8.21 | 14.74 | 4.67 | 7.23 | 1.11 | 5.0 % |
| | *CoV* | 13 % | 8 % | 11 % | 6 % | 13 % | 6 % | 9 % | 4 % | 8 % |
| | *n* | 12 | 6 | 7 | 6 | 8 | 8 | 6 | 8 | 10 |
| S102–6 | *Mean* | 461 | - | 680 | - | 152 | 103 | - | 35 | 60 % |
| | *SD* | 30.40 | - | 54.97 | - | 19.02 | 3.74 | - | 2.36 | 1.3 % |
| | *CoV* | 7 % | - | 8 % | - | 13 % | 4 % | - | 7 % | 2 % |
| | *n* | 8 | - | 7 | - | 8 | 8 | - | 7 | 4 |
| W152–6 | *Mean* | 415 | 93 | 509 | 200 | 166 | 113 | 109 | 38 | 61 % |
| | *SD* | 16.77 | 6.17 | 40.54 | 7.10 | 27.55 | 4.00 | 4.21 | 1.60 | 2.5 % |
| | *CoV* | 4 % | 7 % | 8 % | 4 % | 17 % | 4 % | 4 % | 4 % | 4 % |
| | *n* | 16 | 6 | 14 | 6 | 13 | 8 | 6 | 14 | 6 |

* Standard legend: T-11 (ISO 527–4–1997); T-22 (ISO 527–4–1997); C-11 (EN ISO 14126–2001); C-22 (EN ISO 14126–2001); C-22B (ASTM D695–15); S-12 (ASTM D5379–12); S-21 (ASTM D5379–12); I-31 (EN ISO14130–1998); CA (ISO 1172–1996).

range of 35 mm and aperture ranging from 1.4 to 22, with an accuracy of ± 0.005 mm. The device is placed on a tripod for added stability. One of the key advantages of this approach is the ability to capture strains in various directions within the plane of the specimens, avoiding the need for disposable strain gauges.

Table 3 presents the strength properties[1] determined in these tests, and Table 4 outlines the elastic properties of the SP1, SP2, and SV1 composite materials. The tables are organized based on the direction and type of test (where *x* is the longitudinal (pultrusion) direction, *y* is the in-plane transversal direction, *z* is the out-of-plane direction, and subscripts *c* and *t* refer to a property measured in compression and tension, respectively):

- T-11 and T-22 represent the tensile tests in the longitudinal and transverse directions, respectively. T-11 specimens were tested in the model 5989 UTM, and T-22 specimens in the model 5982 UTM, according to ISO 527–4:1997 [32] (type 2 for T-11 and type 1B for T-22), under displacement control at a rate of 2 mm/min. This test procedure allows determining the in-plane tensile strength in the longitudinal ($f_{x,t}$) and transverse ($f_{y,t}$) directions, the corresponding in-plane tensile moduli ($E_{x,t}$ and $E_{y,t}$) and the in-plane major Poisson ratio in tension ($\nu_{xy,t}$).
- C-11 and C-22 are the compressive tests in the longitudinal and transverse directions, respectively, which were tested in the model 5989 UTM, using the combined loading compression (CLC) method following the standard EN ISO 14126:2001 [15] (type B2 for C-11 and type B1 for C-22), under displacement control, at a rate of 1 mm/min. This test procedure allows determining the in-plane compressive strength in the longitudinal ($f_{x,c}$) and transverse ($f_{y,c}$) directions, the corresponding in-plane compressive moduli ($E_{x,c}$ and $E_{y,c}$) and the in-plane major Poisson ratio in compression ($\nu_{xy,c}$). The failure modes observed in this test are discussed ahead (3.4).
- C-22B is an alternative compressive test method, which was performed in the model 5982 UTM, according to ASTM D695–15 [21],

[1] Notably, vinyl ester resin specimens (C76–6, C152–6, I102–6, L102–6, S102–6, W152–6) showed different strength trends compared to polyester resin specimens (I152–6, L51–5, R140–6), including higher longitudinal compressive strength than tensile strength for vinyl ester resin specimens. These values are higher than other manufacturers' data (*e.g.*, [54]), likely due to differences in fibre architecture and the premium quality material provided by the manufacturer [28], rather than just the type of resin used.

**Table 4**
Elastic properties obtained from coupon tests extracted from the pGFRP profile walls. [mean values, standard deviation (SD), coefficient of variation (CoV) and number of specimens tested ($n$)].

| Profile label | Statistical Parameter | T-11* | | T-22* | C-11* | | C-22* | C-22B* | S-12* | S-21* |
|---|---|---|---|---|---|---|---|---|---|---|
| | | $E_{x,t}$ (GPa) | $\nu_{xy,t}$ (-) | $E_{y,t}$ (GPa) | $E_{x,c}$ (GPa) | $\nu_{xy,c}$ (-) | $E_{y,c}$ (GPa) | $E_{y,c}$ (GPa) | $G_{xy}$ (GPa) | $G_{yx}$ (GPa) |
| C76–6 | *Mean* | 24.2 | 0.263 | - | 23.2 | 0.332 | - | 12.0 | 3.4 | - |
| | *SD* | 0.2 | 0.014 | - | 1.0 | 0.017 | - | 0.7 | 0.2 | - |
| | *CoV* | 1 % | 5 % | - | 5 % | 5 % | - | 6 % | 5 % | - |
| | *n* | 6 | 6 | - | 6 | 6 | - | 6 | 6 | - |
| C152–6 | *Mean* | 27.4 | 0.251 | 11.5 | 25.5 | 0.329 | 10.3 | 10.6 | 3.2 | 3.3 |
| | *SD* | 2.0 | 0.015 | 0.3 | 2.2 | 0.013 | 0.6 | 1.2 | 0.3 | 0.3 |
| | *CoV* | 7 % | 6 % | 2 % | 8 % | 4 % | 5 % | 11 % | 8 % | 11 % |
| | *n* | 14 | 14 | 6 | 13 | 13 | 6 | 12 | 6 | 6 |
| I102–6 | *Mean* | 29.7 | 0.261 | - | 26.5 | 0.330 | - | 10.6 | 3.5 | - |
| | *SD* | 0.6 | 0.010 | - | 0.8 | 0.008 | - | 0.9 | 0.3 | - |
| | *CoV* | 2 % | 4 % | - | 3 % | 3 % | - | 9 % | 9 % | - |
| | *n* | 6 | 6 | - | 6 | 6 | - | 6 | 6 | - |
| I152–6 | *Mean* | 29.8 | 0.285 | 9.6 | 29.1 | 0.313 | 10.0 | 9.3 | 3.1 | 2.3 |
| | *SD* | 7.2 | 0.017 | 0.3 | 5.2 | 0.019 | 0.6 | 2.8 | 0.6 | 0.2 |
| | *CoV* | 24 % | 6 % | 3 % | 18 % | 6 % | 6 % | 30 % | 18 % | 11 % |
| | *n* | 15 | 15 | 6 | 17 | 15 | 6 | 14 | 8 | 6 |
| L51–5 | *Mean* | 24.4 | 0.304 | - | 23.4 | 0.317 | - | 4.9 | 3.3 | - |
| | *SD* | 2.4 | 0.012 | - | 3.4 | 0.014 | - | 0.3 | 0.5 | - |
| | *CoV* | 10 % | 4 % | - | 15 % | 5 % | - | 6 % | 15 % | - |
| | *n* | 6 | 6 | - | 6 | 6 | - | 6 | 6 | - |
| L102–6 | *Mean* | 27.4 | 0.252 | - | 26.4 | 0.343 | - | 11.9 | 2.7 | - |
| | *SD* | 1.9 | 0.013 | - | 2.8 | 0.017 | - | 0.9 | 0.1 | - |
| | *CoV* | 7 % | 5 % | - | 11 % | 5 % | - | 7 % | 5 % | - |
| | *n* | 8 | 8 | - | 8 | 8 | - | 8 | 6 | - |
| R140–6 | *Mean* | 33.7 | 0.280 | 9.0 | 30.9 | 0.325 | 10.3 | 10.0 | 2.9 | 2.0 |
| | *SD* | 6.0 | 0.021 | 0.8 | 6.0 | 0.029 | 1.5 | 1.7 | 0.2 | 0.1 |
| | *CoV* | 18 % | 8 % | 9 % | 19 % | 9 % | 15 % | 17 % | 8 % | 6 % |
| | *n* | 12 | 12 | 6 | 8 | 8 | 6 | 8 | 8 | 6 |
| S102–6 | *Mean* | 29.3 | 0.245 | - | 28.5 | 0.343 | - | 9.7 | 4.6 | - |
| | *SD* | 1.3 | 0.009 | - | 2.3 | 0.025 | - | 1.1 | 0.7 | - |
| | *CoV* | 4 % | 4 % | - | 8 % | 7 % | - | 11 % | 14 % | - |
| | *n* | 8 | 8 | - | 8 | 8 | - | 6 | 8 | - |
| W152–6 | *Mean* | 27.5 | 0.247 | 12.0 | 25.7 | 0.349 | 13.3 | 13.8 | 4.0 | 3.8 |
| | *SD* | 1.5 | 0.015 | 0.3 | 1.0 | 0.013 | 1.1 | 2.2 | 0.4 | 0.3 |
| | *CoV* | 6 % | 6 % | 3 % | 4 % | 4 % | 8 % | 16 % | 11 % | 8 % |
| | *n* | 16 | 16 | 6 | 14 | 14 | 6 | 12 | 8 | 6 |

* Standard legend: T-11 (ISO 527–4–1997); T-22 (ISO 527–4–1997); C-11 (EN ISO 14126–2001); C-22 (EN ISO 14126–2001); C-22B (ASTM D695–15); S-12 (ASTM D5379–12); S-21 (ASTM D5379–12); I-31 (EN ISO14130–1998); CA (ISO 1172–1996).

under displacement control at a rate of 1.3 mm/min. In the transversal direction, this test procedure allows determining the in-plane compressive strength ($f_{y,c}$) and the in-plane compressive modulus ($E_{y,c}$) in the transversal direction. This test procedure was adopted only for profiles that lacked sufficient width for a CLC coupon specimen (profiles C76–6, I102–6, L51–5, L102–6, and S102–6).

- S-12 and S-21 are shear tests in planes *x-y* and *y-x*, respectively, performed in the model 5982 UTM, using the Iosipescu test (V-notched beam method) according to ASTM D5379–12 [33], under displacement control at a rate of 2 mm/min. This test procedure provides the in-plane shear strengths ($f_{xy,v}$ and $f_{yx,v}$) and moduli ($G_{xy}$ and $G_{yx}$). For profiles that lacked sufficient width to test an S-12 specimen (profiles C76–6, I102–6, L51–5, L102–6, and S102–6), it was only possible to do the S-21 test.
- I-31 is the interlaminar shear test in the *z-x* plane, also performed in the model 5982 UTM, with the short-beam method according to ISO 14130:1998 [34], under displacement control at a rate of 1 mm/min. This test procedure allows determining the apparent interlaminar shear strength in the *z-x* plane ($f_{zx,ILS}$).
- CA is the burnout test according to the calcination method following ISO 1172:1996 [35] (method A), performed in a muffle furnace up to 650 °C for 3 hours. This test procedure provides the inorganic weight content of the composite material ($w$%), including both fibres and fillers.

### 2.3. Stub column tests

The stub column specimens used in this study were carefully prepared to obtain surface ends as flat as possible. A rectification process was employed to minimize irregularities resulting from the cutting process, that could promote stress concentrations (due to lack of flatness of end edges) and lead to premature failure of the section walls (avoiding what was reported in previous tests [18]). The flatness and parallelism of the surface ends was quantified with high precision geometric measurements. In those surfaces, the coordinates of 42 points were measured (21 points per surface) with a 3D coordinate measuring machine (CMM). More information about the setup and the measurements is given in Lazzari et al. [36]. Based on the measurements, it was possible to extract the error in parallelism, evaluated as the difference of the maximum and minimum distances between a linear fitted plane in one end surface, compared to the points in the other plane (the results obtained are discussed ahead).

Fig. 2 exemplifies the apparatus and experimental configuration employed for the stub column tests. The tests were conducted in three

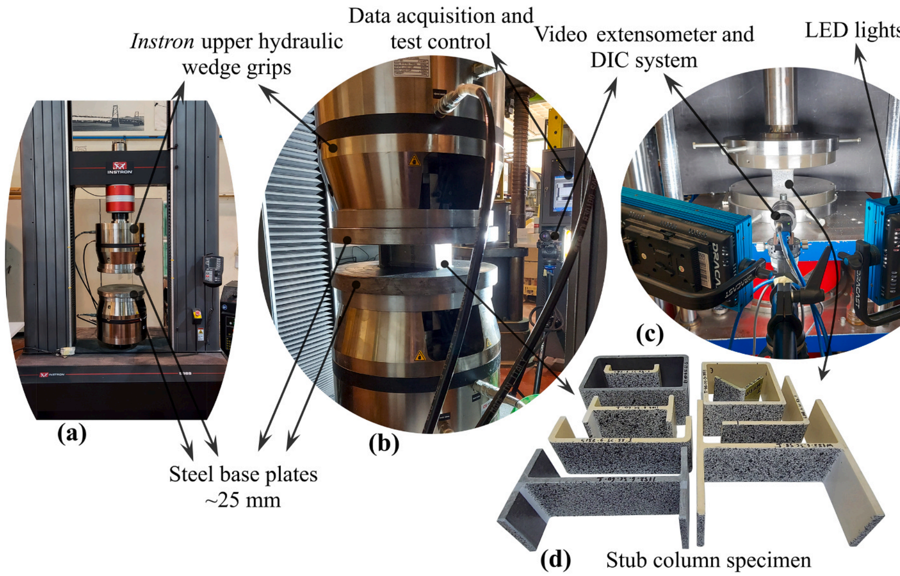


**Fig. 2.** Example of setup for stub column compression tests: (a) UTM 600 kN; (b) stub column test of CI6 series (UTM 600 kN); (c) DIC system with specimen C76–6 (UTM 1200 kN); (d) stub column specimens (SP1, SP2 and SV1) with speckle pattern.

different machines, to cope with a wide range of predicted ultimate loads of the various profiles, namely: two UTMs from Instron with capacities of 600 kN (model 5989) and 1200 kN (SATEC series), and a Hydraulic press from Seidner Form Test with capacity of 3 MN. Steel round flat base plates with thickness of 25 mm were clamped to both crossheads of the UTMs to ensure pure compression testing. The quasi-static tests on the UTMs were performed under displacement control at a rate of 1.00 mm/min, while the tests on the hydraulic press were conducted under load control at a rate of 3 kN/s.[2] All tests were concluded within a period between 2 and 6 minutes, corresponding to the point when the ultimate load was achieved, and the failure mode was assessed.

Certain specimens were equipped with strain recording devices, including strain gauges, video-extensometer targets, and a speckle pattern for DIC measuring. In three specimens of CI6 series, strain gauges were strategically placed at the mid-height of the specimen to record axial strains on the flanges and web. All CI6 specimens (excluding CI6–6) were marked with various target points on the walls, to allow assessing the deformations with a video-extensometer (the same equipment used for the coupon tests). Furthermore, in one specimen from each series, a speckle pattern was applied to one of the flat walls using black Montana® *granit* effect spray (applied over a white matte paint) for strain and displacement acquisition through a 2D DIC system (single camera), as illustrated in Fig. 2(d).

The DIC system consists of a Flir® Blackfly camera connected to a Fujinon® 12.5 mm lens with a 5 MP resolution, which was securely positioned on a cross arm for enhanced stability. The system is linked to a trigger box that synchronizes the force and displacement from the UTM with the captured displacements and strains. During the tests, two LED lights with a 302 × 158 mm$^2$ rectangular panel were used to minimize background noise in DIC images. The software employed for capturing and post-processing the imaging data was MatchID® [37]. Further specifications about the hardware and software setting parameters for automatic strain calculation are detailed in the Appendix (Table A.1). Prior to initiating the strain measurements, the DIC system underwent calibration using dotted plates to correct lens distortions.

Fig. 3 illustrates the configuration of the DIC speckle pattern, positions of video-extensometer (VE) and electrical strain gauges (SG). The VE and SG were positioned at the midpoint of the specimen length, equally spaced along the transversal direction of the web by 34.9 mm; in the flanges, the SG were spaced by 19.1 mm. All specimens had VE points, while only specimens CI6–4, CI6–5 and CI6–6 had SGs; specimen CI6–6 had a speckle pattern for 2D strain acquisition using DIC (Fig. 3).

It is important to mention that the stub column tests were performed according to recommendations of previous studies [18,38], and also according to the recent standard procedure for full-section compression tests on pultruded profiles (ISO 23930 [14]), which specifies a similar procedure to that described in Annex B of GB/T 31539 [39].

To guarantee that the columns were in fact stub, their length was determined so that the critical buckling load was significantly higher than the (predicted) material's crushing load. Cardoso et al. [40] suggested that material crushing failure in columns and plates can be predicted when both the relative plate slenderness ($\lambda_L$) and relative column slenderness ($\lambda_G$) are below 0.7. Slenderness ($\lambda$) was calculated as the square root of the ratio between the material's compressive strength ($f_c$) and the critical buckling stress ($f_{cr}$), *i.e.*, $\lambda = (f_c / f_{cr})^{0.5}$. The critical buckling stresses, corresponding to local and global buckling modes, were obtained from elastic buckling analysis using *FStr* software [41], by means of a finite strip method (FSM) [42], which provides the solution of a generalized eigenvalue problem. The use of computational solutions, such as the FSM, has already been proven to provide a flexible, fast, and precise estimate of the critical buckling stresses for orthotropic materials [43–47]. In the *FStr* software, the boundary conditions were considered clamped-clamped[3] and 10 halfwave length terms were used. The material's compressive strength was first determined from coupon tests (*i.e.*, $f_c = f_{x,c}$). From the compressive strength and the slenderness limit (*e.g.*, $\lambda_{lim} = 0.7$, according to Cardoso et al. [40]), the limit critical stress associated with a specific longitudinal length ($L$) could then be

[2] For one of the sections (S102–6), tests were carried out under both load control and displacement control; these tests yielded equivalent results in terms of load *vs*. cross-head displacement, failure mode and maximum load, thereby validating the procedure.

[3] The contact between the bearing plates and the wall edges of column end sections under compression leads to a high rotational restraint that increases with the wall thickness and compression level. Although the real end boundary condition is neither perfectly fixed nor simply supported, a fixed configuration is assumed for sake of simplicity (the exact value of rotational stiffness would be rather difficult to compute because it would depend on the interaction between thickness and compression level).

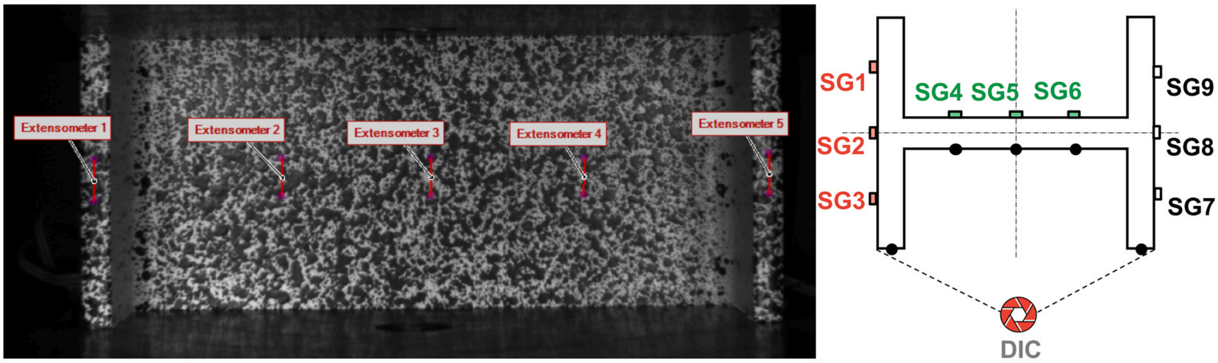


**Fig. 3.** DIC, VE direction zones and SG positions for strain measurements.

**Table 5**
Five-stage description of the experimental campaign (*n* is the number of specimens used in each stage).

| Phase | Description | Specimens | *n* | Experimental devices* |
|---|---|---|---|---|
| *Stage 1* | Measurements of end surfaces flatness | CI6–6 | 1 | 3D CMM |
| *Stage 2* | Axial load/stress vs. strain behaviour | CI6–1, CI6–2, CI6–3 | 3 | UTM 600 kN, VE |
| | | CI6–4, CI6–5 | 2 | UTM 600 kN, SG, VE |
| | | CI6–6 | 1 | UTM 600 kN, SG, DIC |
| | | First series of SP1, SP2 and SV1 material | 9 | UTM 1200 kN and DIC |
| *Stage 3* | Effect of local relative slenderness | C76–6 series | 15 | UTM 600 kN |
| | | I102–6 series | 15 | UTM 600 kN |
| | | S102–6 series | 15 | HP 3 MN |
| *Stage 4* | Full-section compressive strength of various cross-sections | All data (without the ISO 23930 specimens) | 92 | UTM 600 kN, UTM 1200 kN, and HP 3 MN |
| *Stage 5* | Correlation matrix | All data (without the ISO 23930 specimens) | 92 | UTM 600 kN, UTM 1200 kN, and HP 3 MN |

* CMM: 3D Coordinate measuring machine; UTM: Universal testing machine; SG: Strain gauge; VE: Video-extensometer; DIC: Digital image correlation system; HP: Hydraulic press

calculated. By considering the material elastic properties presented in Table 4 as input for the elastic buckling analysis, a target limit length could be defined for the stub specimens corresponding to the different cross-sections.

A total of 101 stub column specimens were tested and analysed, in a five-stage process, as summarized in Table 5, and detailed as follows:

(i) Measurements of end surface flatness (3.1): In the first stage, the flatness of the end surfaces of CI6–6 specimen was evaluated using a CMM equipment to assess the quality of the rectification process.

(ii) Axial load/stress vs. strain behaviour (3.2): The second stage involved the study of the load *vs.* strain behaviour. Initially, six specimens of profile CI6 were tested, with a maximum length of 64 mm ($\lambda_{lim} = 0.7$), to evaluate such behaviour and to validate the readings provided by the video-extensometer and the DIC system against "conventional" electric SG. After validation, in one specimen of each series, the strain distribution was acquired using the DIC system.

(iii) Effect of local relative slenderness (3.3): The third stage involved testing 45 specimens (C76–6, I102–6 and S102–6), which were used for a parametric study with the objective of evaluating the ultimate capacity of stub columns under a range of low slenderness values ($0.4 < \lambda_{lim} < 0.7$). For this experimental parametric study, using the C76–6, I102–6 and S102–6 profiles, each cross-section was tested with 5 different lengths: (1) four lengths were chosen based on a set of 4 slenderness values (*i.e.*, $\lambda_{lim}$ = [0.4; 0.5; 0.6; 0.7]), (2) one length was chosen according to the limitations included in the ISO 23930 [14], (3) 3 repetitions were made for each length, and (4) no strain data was recorded, only the ultimate compressive load was registered (more information about the critical buckling load and length of the specimens is provided in Table A.2 of the Appendix).

(iv) Full-section compressive strength of various cross-sections (3.4): In a fourth stage, the ultimate load was determined for 11 types of profiles provided by three manufacturers, totalling 92 specimens. A subset of these specimens underwent evaluation of the failure mode compared to the CLC coupon tests.

(v) Correlation matrix (3.5): In the last stage, a correlation matrix was generated to evaluate possible correlations between the experimental data. This analysis provided insights into the linear dependency or independency between the experimental variables, involving geometrical, elastic and strength properties, from coupon and stub column tests.

## 3. Results and discussion

### 3.1. Measurements of end surface flatness

As mentioned, the out-of-plane defects, flatness, and parallelism of the surface ends were assessed using a 3D CMM equipment. These measurements were conducted on CI6–6 specimen and the results are presented in Fig. 4, which depicts the global coordinates of the measured points, along with the local out-of-plane values measured with respect to the centroid of the cross-section.

It can be seen that the out-of-plane values at the extremities were very low, with a maximum value of 0.101 mm (top plane) and a minimum value of −0.087 mm (bottom plane). The error in parallelism was found to be 0.093 mm, well below the limit deviation defined in ISO 23930 [14], of 0.5 mm. Additionally, the parallelism in degrees was evaluated as 0.038º, and the flatness of each end surface was measured as 0.035 mm and 0.058 mm.

These results indicate that the error in parallelism of the end surfaces in contact with the end plates of the machine is very low, amounting to around 20 % of the maximum limit proposed by ISO 23930 [14]. Moreover, this measurement validates the rectification process adopted in the experimental campaign and applied to all specimens.

It is important to mention that previous studies [16–20] have identified end-surface imperfections as one of the possible explanations for

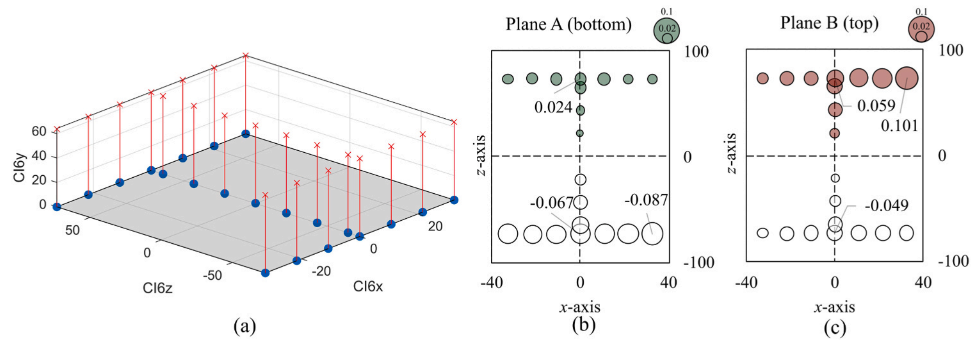

**Fig. 4.** Geometric measurements of end cut surface points of specimen CI6–6: (a) global coordinates, (b) bottom plane defects and (c) top plane defects.

the lower full-section compressive strength, when compared to its coupon counterparts, justifying the care taken in the preparation of the test specimens in the present study. In practical applications, namely on construction job sites, it is likely not feasible to adopt the rectification process used in the experiments. Such a meticulous procedure for end surfaces rectification has been adopted here to evaluate the "pure" crushing phenomenon, namely to minimize the possibility of premature failure of the stub columns due to irregularities caused by the cutting process. In fact, understanding the "pure" crushing phenomenon of pGFRP profiles is fundamental for developing precise and reliable provisions for engineering design practice.

### 3.2. Axial load/stress vs. strain behaviour

Fig. 5 illustrates the axial load *vs.* strain behaviour, with strains being measured using SGs for specimens CI6–4, CI6–5 and CI6–6. As previous stated, three SGs were strategically attached at mid-length of the specimens, in the web and flanges, following the positions outlined in ISO 23930 [14] (SG1, SG5 and SG7 in Fig. 3). A similar behaviour between each specimen is evident from the consistent slope observed in the elastic region of the load *vs.* strain curve derived from the strain measurements obtained from the web and flanges of the profile.

One notable observation from Fig. 5 is the presence of a nonlinear behaviour during the initial stage of the test, for compressive loads spanning from 0 kN to 50 kN. This phenomenon can be attributed to a similar physical effect described in ASTM D695–15 [21]. The possible causes for this behaviour include the irregular flatness of the specimen's end surfaces (or of the steel plates of the test apparatus, which may be non-perfectly parallel), or the potential misalignment of the specimen w.r.t. the testing machine. Despite the efforts to ensure the centring of the specimens and end edges flatness, small imperfections and material heterogeneity inevitably influence the stress distribution and

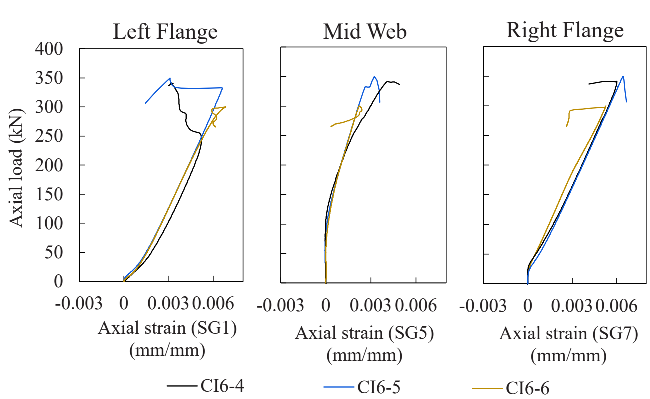

**Fig. 5.** Axial load *vs.* axial strain behaviour of CI6–4, CI6–5 and CI6–6 stub columns; strains measured with strain-gauges (SG) placed at the same positions (left flange SG1, mid-web SG5 and right flange SG7).

subsequently affect strains. However, it is important to note that this nonlinear effect is primarily observed in the initial stage of the tests. Subsequently, a distinct region of linear behaviour, for loads ranging from 100 kN to 250 kN, becomes prominent, with the web being the last section wall to be loaded: in fact, deformations only start to increase significantly after an average compressive load of 100 kN is reached. This linear region was considered sufficiently extensive to determine the full-section longitudinal compressive modulus of the profile.

Fig. 6 displays the validation of the DIC strain data against the SGs data. The axial strain data from the DIC (extracted as extensometers) were collected from points adjacent to the nearest SG, as depicted in Fig. 3. It is evident that, within the elastic range, the strain distribution obtained using the two alternative methods was highly consistent. Upon reaching the maximum load, a slightly nonlinear behaviour emerged, which was attributed to material nonlinear effects, including delamination.

Regarding the stiffness measurements of the stub columns, Fig. 7 presents the apparent values of the "local" longitudinal compressive modulus obtained for each specified target line using the VE. Considering all tested specimens of series CI6, a mean value of the full-section longitudinal compressive modulus of 29.5 GPa (CoV of 13 %) was obtained from the "local" estimates, weighted based on their respective widths of influence. The "local" estimates of the compressive modulus revealed notable consistency for the target alignments in the flanges, with coefficients of variation (CoV) around ~10 %. In contrast, the target alignments in the web exhibited significantly higher dispersion (CoV between 12 % and 27 %), especially in the central alignment (zone 3), where two of the measured values were much larger than their counterparts. Finally, the comparison between the compressive moduli presented in Fig. 7 with those obtained from coupon tests in previous studies [18,30] shows that the coupon tests provide lower average values than the full-section tests (11–36 % lower).

In what concerns the comparison between the axial stress *vs.* strain behaviour of the stub column and CLC coupon tests, Fig. 8(a) presents a typical result for the C76–6 cross-section (identified as specimen C76-6-SC-59–1 in Table A.2). The strains from the stub column tests were taken from the midpoint length of the C76–6 web at three different positions along the transversal direction (equally spaced), as depicted in Fig. 8(b). The results of the axial deformation of the web of this stub column were very consistent, showing linear elastic behaviour. The same behaviour was observed for the coupon tests. Conversely, the ultimate load for the stub column tests was much lower, around 60 % of the strength given by the CLC coupon test.

Fig. 8(b) and Fig. 9(a) illustrate a typical example of a 2D-DIC longitudinal (axial) displacement field (*x*-direction) of the C76–6–1 specimen. The evolution of the axial displacement field (Fig. 9(a)) shows a relatively uniform load distribution along the cross-section after the initial stage of "settlement". Similarly, the axial strain field evolution (Fig. 9(b)) indicates an almost constant value along the section wall up to failure. In conclusion, the results obtained from the 2D-DIC analysis

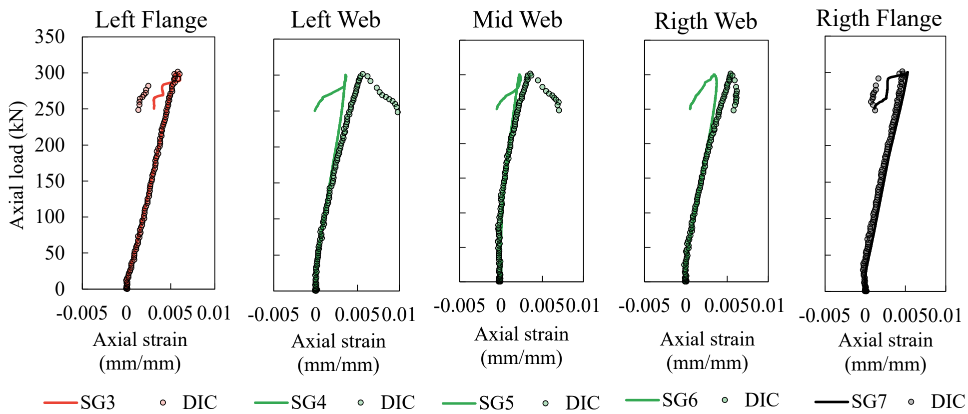


**Fig. 6.** Comparison of strain gauge (SG) data with DIC data at opposing wall positions of CI6–6 specimen.

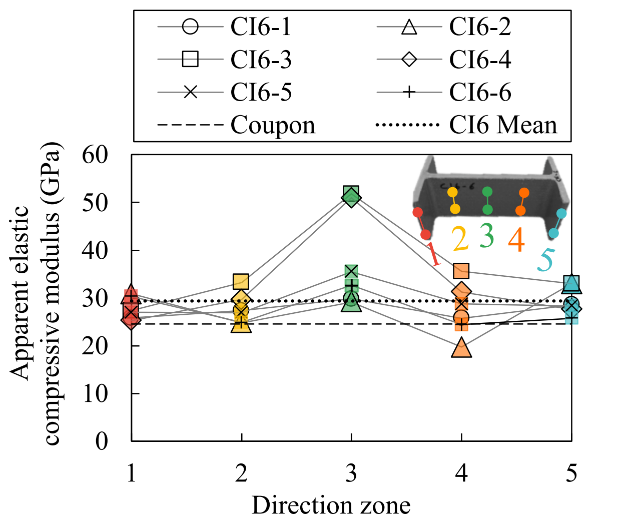


**Fig. 7.** Values of apparent longitudinal compressive moduli, obtained from the stub column tests, series CI6.

provided consistent information about the 2D axial displacement/strain field. Moreover, the careful visual inspection of the specimens allowed concluding that buckling did not occur, and the applied load was uniformly distributed, thereby confirming the occurrence of pure material crushing failure.

### 3.3. Effect of local relative slenderness

The parametric study presented in this section investigates stocky pGFRP columns with local relative slenderness ratios ranging from 0.4 to 0.7. The objective is to examine the influence of column slenderness on the ultimate capacity of stub columns and to determine the threshold slenderness for which material crushing failure occurs without influence of buckling phenomena.

Table 6 presents the strength of the stub columns tested within this study, and Table A.2 of the Appendix presents detailed information about each tested specimen. As mentioned in Table 5, only Sections C76–6, I102–6 and S102–6 were used in this part of the study. For each type of cross section and specimen length, Table 6 indicates the full-section compressive strength of the stub column ($f_{SC}$) and compares it to the in-plane longitudinal compressive strength obtained from coupon tests ($f_{x,c}$), associated to each local relative slenderness ratio λ. The ratio of stub column compressive strength to coupon compressive strength (also called strength reduction factor, $\chi = f_{SC} / f_{x,c}$) ranged from 0.45 to 0.69. Furthermore, specimens C76–6, I102–6, and S102–6, which share the same manufacturer and constituent materials (see Table 1 and Table 2), exhibited an average compressive strength (from coupon tests) of 597 MPa with CoV of 14 %, while the stub column tests yielded an average strength of 341 MPa with CoV of 5 %. This finding is in line with previous studies [16–20].

Fig. 10 illustrates a graphical relationship between the strength reduction factor (χ) and the slenderness ratio (λ) for the tested specimens. The strength reduction factor χ and the relative slenderness λ are taken from Table 6. The critical buckling stress ($f_{cr}$) used to compute the relative slenderness was obtained from the *FStr* software [41], which

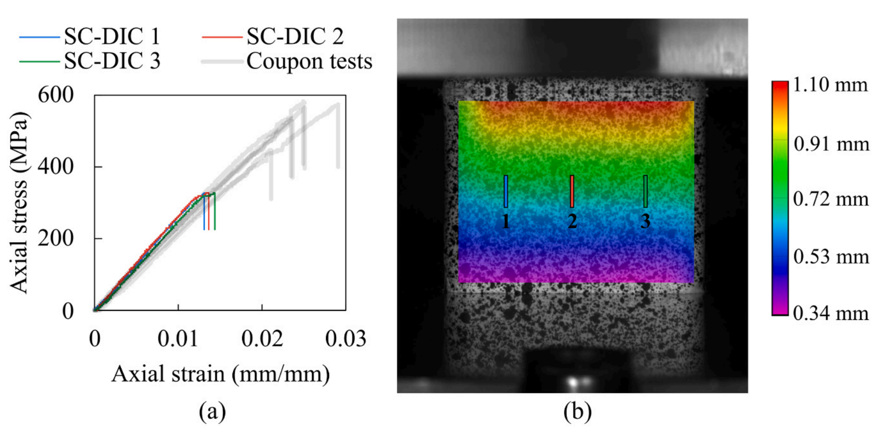


**Fig. 8.** Typical results of a DIC system from series C76–6: (a) axial stress *vs.* strain compressive behaviour of stub column (SC) and CLC coupon tests, and (b) displacement field in longitudinal direction at average ultimate strength of 326 MPa (ultimate load 216 kN).

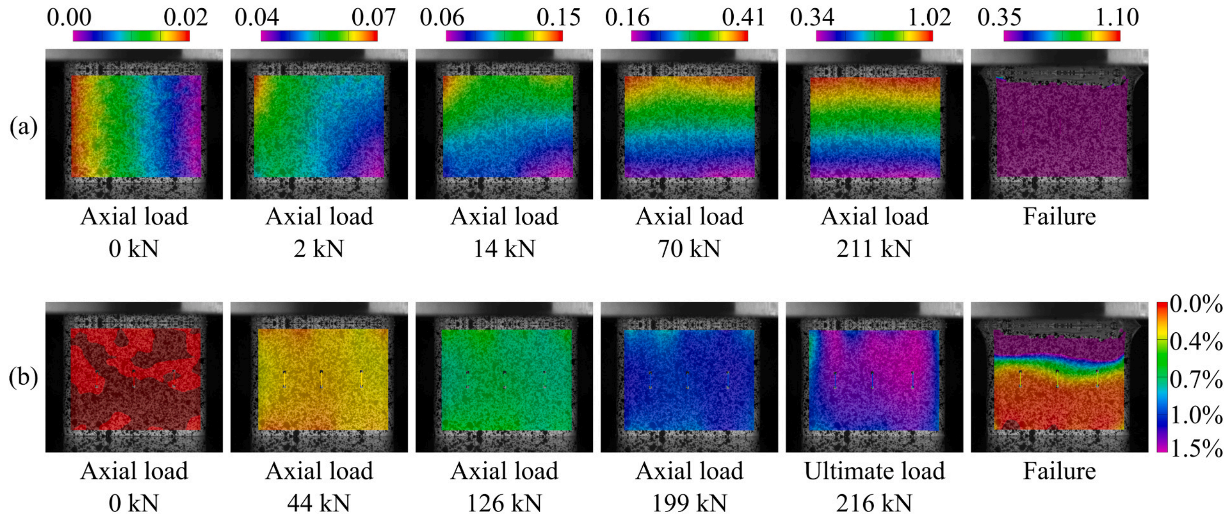


**Fig. 9.** Typical results of a 2D-DIC fields from stub column series C76–6: (a) axial displacement field (mm) and (b) axial strain field.

**Table 6**
Strength results of stub column tests ($f_{SC}$) and comparison with CLC coupon tests ($f_{x,c}$) (where $L$ is the member length, $f_{cr}$ is the critical buckling stress, $n$ is the number of specimens and λ is the relative slenderness).

| Specimen | $L$ (mm) | $f_{cr}$ (MPa) | *Stub Columns* | | | | *Coupons* | | | | $\chi = f_{SC}/f_{x,c}$ |
|---|---|---|---|---|---|---|---|---|---|---|---|
| | | | $n$ | $f_{SC}$ (MPa) | | λ | $n$ | $f_{x,c}$ (MPa) | | λ | |
| | | | | *Mean* | *CoV* | | | *Mean* | *CoV* | | |
| C76–6–17* | 17* | 3409 | 3 | 366 | 2 % | 0.33 | 5 | 561 | 4 % | 0.41 | 0.65 |
| C76–6–30 | 30 | 3275 | 3 | 363 | 0 % | 0.33 | 5 | 561 | 4 % | 0.41 | 0.65 |
| C76–6–40 | 40 | 2197 | 3 | 342 | 3 % | 0.39 | 5 | 561 | 4 % | 0.51 | 0.61 |
| C76–6–49 | 49 | 1541 | 3 | 347 | 2 % | 0.47 | 5 | 561 | 4 % | 0.60 | 0.62 |
| C76–6–59 | 59 | 1134 | 3 | 359 | 2 % | 0.56 | 5 | 561 | 4 % | 0.70 | 0.64 |
| I102–6–31* | 31* | 3500 | 3 | 325 | 1 % | 0.30 | 5 | 515 | 6 % | 0.38 | 0.63 |
| I102–6–33 | 33 | 3179 | 3 | 326 | 5 % | 0.32 | 5 | 515 | 6 % | 0.40 | 0.63 |
| I102–6–41 | 41 | 2103 | 3 | 328 | 6 % | 0.39 | 5 | 515 | 6 % | 0.50 | 0.64 |
| I102–6–50 | 50 | 1451 | 3 | 349 | 4 % | 0.49 | 5 | 515 | 6 % | 0.60 | 0.68 |
| I102–6–60 | 60 | 1045 | 3 | 358 | 2 % | 0.58 | 5 | 515 | 6 % | 0.70 | 0.69 |
| S102–6–117* | 117* | 413 | 3 | 304 | 1 % | 0.86 | 7 | 680 | 8 % | 1.28 | 0.45 |
| S102–6–32 | 32 | 3585 | 3 | 325 | 4 % | 0.30 | 7 | 680 | 8 % | 0.43 | 0.48 |
| S102–6–37 | 37 | 2741 | 3 | 331 | 5 % | 0.35 | 7 | 680 | 8 % | 0.50 | 0.49 |
| S102–6–45 | 45 | 1894 | 3 | 315 | 3 % | 0.41 | 7 | 680 | 8 % | 0.60 | 0.46 |
| S102–6–54 | 54 | 1356 | 3 | 355 | 3 % | 0.51 | 7 | 680 | 8 % | 0.70 | 0.52 |

[*] Longitudinal length according to ISO 23930, $L = 3r$ (where r is the minor radius of gyration) and $L < 5t$ (for walls with free edges, when it is possible, due to limitation of the profile dimension).

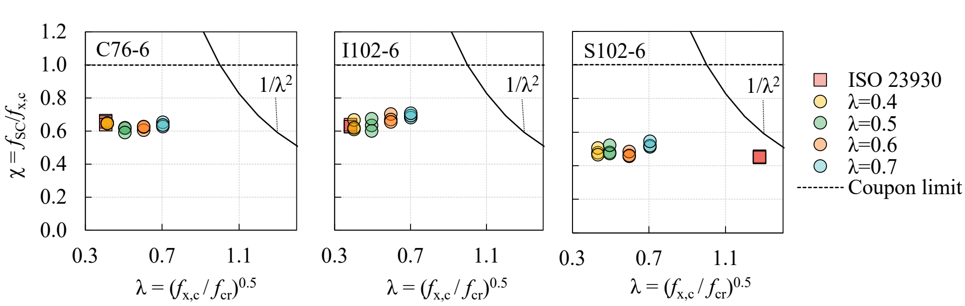


**Fig. 10.** Strength reduction factor (χ) *vs.* relative local slenderness ratio (λ) of pultruded GFRP stub column tests C76–6, I102–6 and S102–6, including those prepared according to ISO 23930 [14] standard.

identified local buckling as the critical mode.

Fig. 10 shows that the value of the strength reduction factor is much lower than 1.0. Additionally, for each cross-section, there is a plateau which indicates that the stub column resistance was limited by the corresponding material's compressive strength (when λ < 0.7). However, it is important to note that the different cross-sections present distinct plateaus. This may be attributed to the influence of cross-section geometry on material crushing behaviour, including different strain behaviour for different cross-sections, and also differences in fibre-architecture, wall thickness, weaker wall junctions and material heterogeneity resulting from the pultrusion process (as mentioned, although great care was taken in the preparation of end surfaces and specimen alignment in the test machine, small irregular flatness of the specimens or misalignment of the profile within the testing machine might also be a cause for this behaviour).

Another relevant aspect for discussion is the standard procedure defined in ISO 23930 [14] for determining the full-section compressive strength, which prompts a few remarks. Firstly, the standard requires a test speed equivalent to 10 % of the specimen's longitudinal length by minute. However, this test speed may be excessively high for capturing the material crushing behaviour in a quasi-static stub column test (*e.g.*, 11.7 mm/min for the S102–6–117 specimens, in addition to a total test time below 1 min for specimens C76–6–17 and I102–6–31). Secondly, the standard imposes restrictions on width-to-thickness ratio to prevent second order effects, which is based on a "pure" geometric slenderness, instead of a relative slenderness. To prevent global buckling, the geometric slenderness ratio is defined in ISO 23930 [14] as the length divided by the minor radius of gyration, and it must be less than 3. Similarly, to avoid local buckling, the width-to-thickness ratio (where width is the larger dimension between the length of the stub column and the wall's cross-section width) should be below specific thresholds, according to the side support boundaries of the plates and section symmetry: (i) 5 for outstanding walls, (ii) 8 for internal walls, and (iii) 5 for non-double symmetrical sections. It is important to note that these limitations do not take into account the elastic and strength properties of the materials, thus potentially resulting in inaccurate estimates of the maximum length required to prevent buckling phenomena.

Fig. 10 clearly demonstrates that specimens complying with the provisions given in ISO 23930 [14] may result in inadequate slenderness values, not representing the actual intended slenderness of the structural member. In particular, the S102–6–117 specimen (ISO 23930) closely aligned with the pure buckling curve ($1/\lambda^2$), implying a potential interaction between crushing and buckling. The slenderness limitations outlined in the aforementioned standard could be more accurately defined if the material properties were taken into consideration (*e.g.* obtained using the CLC standardized procedure for coupon testing). However, as mentioned, defining the actual material strength is quite challenging. Using CLC coupon tests for predicting the axial compressive resistance to crushing of full-section pGFRP profiles is notably non-conservative. On the other hand, defining the relative slenderness based on this strength prediction is conservative (around 10 % lower, as illustrated in Table 6). In other words, by limiting the relative slenderness to 0.7 using CLC coupon tests as an initial estimate of material failure, it is expected that the actual slenderness is lower than 0.7, given that the real full-section compression strength to crushing is lower than the in-plane compressive strength from CLC coupon tests.

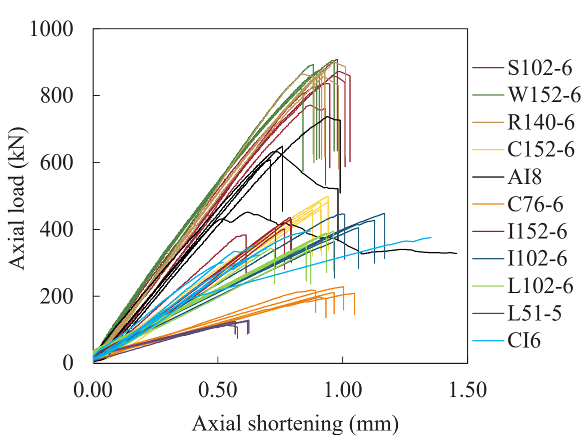


**Fig. 11.** Axial shortening *vs.* axial load of the tested stub columns under displacement control.

### 3.4. Full-section compressive strength of various cross-sections

Fig. 11 displays the axial force *vs.* axial shortening curves for all tested specimens. The curves exhibit nearly linear elastic behaviour up until the point of abrupt and brittle failure. The absence of a slightly nonlinear curve prior to reaching maximum load suggests that there is no drop in axial stiffness, indicating no local buckling. This characteristic behaviour was consistently observed across all 92 tested specimens, confirming the occurrence of "pure" material crushing failure. All the tests of the same series have shown similar behaviour, while specimens from different series and different geometries present differences in both ultimate capacity and initial stiffness. It is worth noting that the initial nonlinear stage observed in the axial force *vs.* cross-head displacement is a prevalent occurrence in tests involving intricate contact surfaces. To mitigate this effect, the real axial force *vs.* axial shortening was obtained by subtracting the elastic deformation of the UTM conducting an "empty" test.[4]

Fig. 12 illustrates, as an example, the typical failure mode of the stub columns from the Strongwell material series. Typically, in all cases, material failure phenomenon has been identified. The specific failure modes observed in the stub columns were classified according to ISO 23930 [14], ASTM D6641–14 [12], and Opelt et al. [13], being listed in Table 7. ISO 23930 [14] provides five types of classifications, of which three are valid (material rupture, delamination, junction failure) and two are invalid (global buckling and local buckling, which are not correctly defined according to the theory of elastic stability). The failure modes classification according to Opelt et al. [13] includes two main groups: failure type and failure mode. As shown, several combinations of failure modes were identified. According to Opelt et al. [13], the combination of several modes can be defined as "multiple failure modes" when irregular fracture propagation develops in the width (in-plane) direction.

Concerning the failure modes observed in the coupon tests, illustrated in Fig. 13 and Table 8, several noteworthy observations can be made. Essentially, coupon tests exhibit in some cases a "mixed failure mode", where the fracture irregularly propagates through the thickness direction. In contrast, the stub columns demonstrate "multiple failure modes" and "mixed failure modes", according with the definition of Opelt et al. [13]. The complexity of failure modes is evident at the laminate scale, and this complexity becomes even more pronounced at the full-section scale, highlighting the heterogeneity of the material.

It is evident that the full-section of the profiles and the associated size effects of the geometry result in an interaction of several localized material failures due to the heterogeneity/discontinuity of the material along the transversal direction. This discontinuity in material properties is predominantly found in "singularities", where the section walls intersect each other (*e.g.*, flange-web junction), or where there is an overlap of mats (*e.g.*, hollow sections) or a dead-end of the wall segment (*e.g.*, free-end extremity of a C-section flange). These "singularities" do not exist in coupons, which are usually extracted from the central part of the section walls (as defined in EN 13706–2 [48]). This interaction between several failure modes (defined as "multiple failure modes") is probably one of the main causes of the high discrepancy between the (full-section) compressive strength determined in the stub column tests

[4] This procedure involved an initial test without any specimen, comprising only the compression between the end plates, up to 50 % of the maximum capacity of the UTM. This procedure provided the axial force *vs.* cross-head displacement of the UTM. This information is related to the machine deformation that occurs during the initial stages of loading, as well as the elastic deformation for higher loads. With this "baseline" data, it is possible to obtain the actual axial displacement of the stub columns by subtracting the displacement from the empty test from that of a stub column test. This procedure is useful when comparing experimental results with computational simulations, thereby streamlining the calibration analysis.

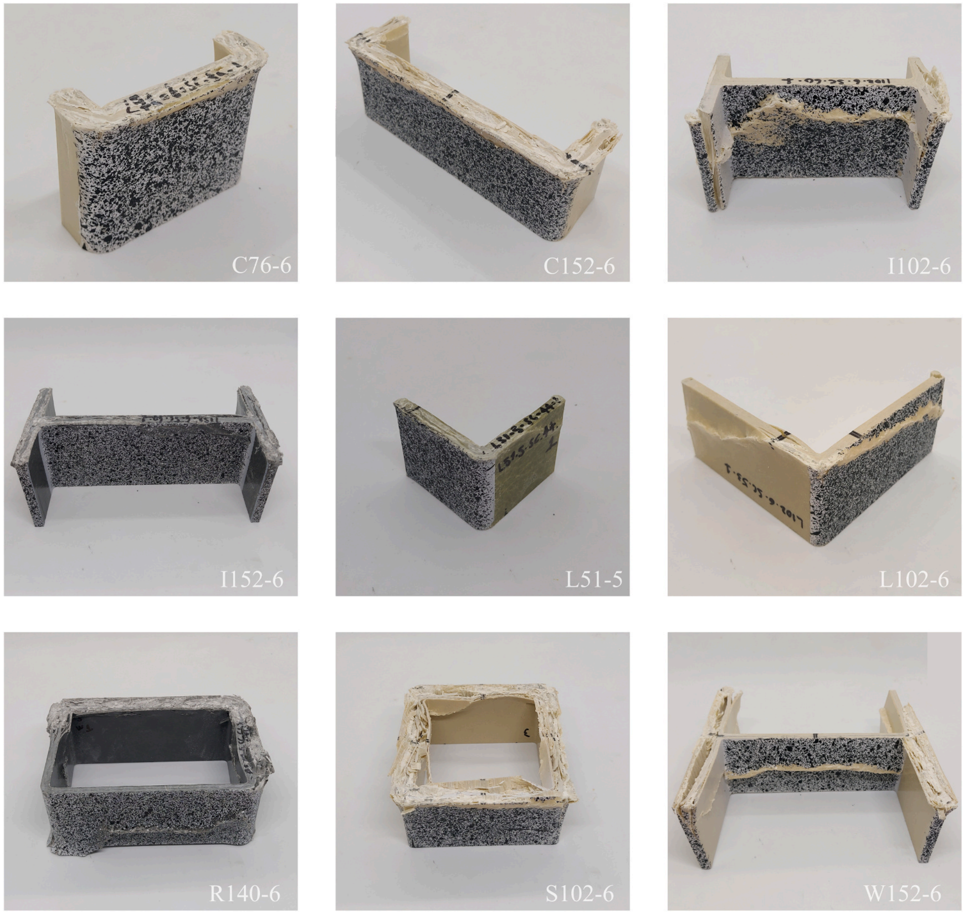


**Fig. 12.** Stub columns failure modes for the first series of Strongwell material.

compared to that estimated from the CLC coupon tests. As an example, this material discontinuity along the transversal direction is also noticeable through geometrical characterization of the thickness, as illustrated in a previous work [36]. These findings emphasize the relevance of material imperfections at the full-section level induced by the pultrusion process, including the pulling and curing procedures. This material imperfection has also been highlighted in other studies evaluating the occurrence of residual stresses [49], initial geometrical imperfections ("distortions") [49,50], and non-uniform fibre distribution [51,52] resulting from the pultrusion process.

All results of the stub column tests are detailed in Table A.2 (Appendix), categorized by specimen, shape, geometrical parameters, and experimental ultimate stub column load ($P_{SC}$). For clarity, Fig. 14(a) depicts the strength reduction factor ($\chi = f_{SC} / f_{x,c}$) against the relative local slenderness ($\lambda$), excluding specimens conforming to ISO 23930 standard [14]. The graphical representation is categorized by cross-section shape and juxtaposed with the perfect column (PC) curve, defined as $\chi = 1$ when $\lambda \leq 1$ (theoretical compressive crushing plateau), and $\chi = 1/\lambda^2$ for $\lambda > 1$(theoretical elastic local buckling curve). The PC curve is a common base for design proposals (*e.g.*, [5,40]), including those of steel structures, *e.g.*, [53]. The adoption of a strength reduction factor is a conventional practice in designing members subjected to compression. In this context, the experimental ultimate stub column strength is normalized by the CLC compressive strength ($f_{x,c}$), as prescribed by the European Technical Specification CEN/TS 19101:2022 [9] for predicting the resistance to crushing failure.

The primary observation in Fig. 14(a) is the fact that the strength reduction factors obtained were consistently lower than 1.0 ($0.4 < \chi < 0.8$), as previously depicted in Fig. 10, with a mean value of 0.60 and CoV of 15 %. These results indicate that the formula proposed by the current standard [9] does not allow to accurately quantify the resistance to crushing. Therefore, it is evident that a full-section compressive resistance based on the sectional area and on the strength of CLC coupons extracted from the central zones of the walls of pGFRP profiles does not represent the full-section crushing failure phenomenon with sufficient accuracy.

Additionally, Fig. 14(b) presents the results of the present study compared to the available results from the literature[5] [16–20]. The trends clearly show that the reduction factor follows the same behaviour as observed by other authors. Notably, some specimens in the highlighted "crushing zone" are close to $\chi = 1.0$, specifically the circular tubular sections series tested by Al-Saadi et al. [17] and Higgoda et al. [20]. This discrepancy may be attributed to the influence of the circular cross-section geometry on material crushing behaviour, such as, the absence of wall junctions and possibly lower values of coupon compressive tests influenced by the tube curvature in the coupon specimens. On the other hand, the stub columns tested by Wu et al. [19] have an average reduction factor lower than 0.4, which is explained by their higher relative slenderness ($1.0 < \lambda < 1.3$). This indicates that the stub columns reported with crushing failure (with longitudinal lengths less than 200 mm) are indeed outside the "crushing zone," suggesting a range of possible crushing-buckling interactions.

[5] As mentioned in the Introduction, data from [22–26] could not be included in this analysis, due to the absence of standardized mechanical characterization tests on small coupons, such as CLC tests.

**Table 7**
Stub columns failure mode classifications according with ISO 23930 [14], ASTM D6641-14 [12] and Opelt et al. [13].

| Profile label | ISO 23930:2023 | ASTM D6641-14 | Opelt et al. (2018) | |
|---|---|---|---|---|
| | *Failure mode* | *Failure mode* | *Failure type* | *Failure mode* |
| CI6 | Material rupture | End-crushing | Interfacial | Fiber crushing |
| AI8 | Material rupture, junction failure, delamination | Multi-mode (delamination, end-crushing, long-splitting) | Interfacial, interlaminar | Fiber crushing, delamination buckling |
| C76–6 | Material rupture | End-crushing | Interfacial | Fiber crushing |
| C152–6 | Material rupture | End-crushing | Interfacial | Fiber crushing |
| I102–6 | Delamination | Multi-mode (delamination, end-crushing, transverse shear) | Interfacial, interlaminar, shear | Fiber crushing, delamination buckling, in-plane shear, through-the-thickness shear, wedge splitting |
| I152–6 | Material rupture, delamination | Multi-mode (delamination, end-crushing) | Interfacial, interlaminar | Fiber crushing, delamination buckling |
| L51–5 | Material rupture | Multi-mode (delamination, end-crushing) | Interfacial, interlaminar | Fiber crushing, delamination buckling |
| L102–6 | Material rupture | Multi-mode (delamination, end-crushing, transverse shear) | Interfacial, interlaminar, shear | Fiber crushing, delamination buckling, in-plane shear, through-the-thickness shear, wedge splitting |
| R140–6 | Material rupture, delamination | Multi-mode (delamination, end-crushing, transverse shear) | Interfacial, interlaminar, shear | Fiber crushing, delamination buckling, in-plane shear, through-the-thickness shear, wedge splitting |
| S102–6 | Material rupture | Multi-mode (delamination, end-crushing) | Interfacial, interlaminar | Fiber crushing, delamination buckling |
| W152–6 | Material rupture, delamination | Multi-mode (delamination, end-crushing, through-thickness, transverse shear, kink band) | Interfacial, interlaminar, shear, kink-band | Fiber crushing, delamination buckling, through-the-thickness shear, through-the-thickness kink-bands |

### *3.5. Correlation matrix*

The extensive dataset presented in this study allowed conducting a correlation analysis. Fig. 15 shows a graphical illustration of a correlation matrix, with key parameters in view of design procedures highlighted in Fig. 16, displaying Pearson's linear correlation coefficients (**R**, red values indicate correlations higher than 0.2) for the following variables: geometrical parameters, elastic properties, strength properties, experimental stub column maximum compressive load ($P_{SC}$) and strength ($f_{SC}$). While a correlation coefficient of 1.0 is typically shown along the diagonal in correlation matrices, the present matrix features a histogram depicting the frequency of occurrence of the variables analysed. In the other matrix cells, linear regressions are provided for pairs of variables. A correlation coefficient close to 1.0 indicates a robust correlation, implying a linear dependency between the variables. Conversely, a correlation coefficient near zero means a lack of linear dependence (note that even if the correlation coefficient is close to zero, this does not necessary imply complete independence, as non-linear dependencies may still exist). A positive correlation implies a direct linear relationship, while a negative correlation signifies an inverse linear relationship. The results of the correlation matrix can be useful for the development of more accurate design predictions.

Concerning the linear dependency of the full-section compressive resistance, the following observations are made:

(i) As expected, a strong positive linear dependency ($\mathbf{R} = 0.95$) exists between the ultimate stub column load ($P_{SC}$) and the cross-section area.

(ii) Fig. 16 shows that the resistance to crushing, estimated according to CEN/TS 19101:2022 [9] ($N_{c,R1} = f_{x,c}A$) exhibits a strong linear dependency with the stub column load, $P_{SC}$ ($\mathbf{R} = 0.95$). However, this relationship is primarily driven by the strong correlation with the cross-sectional area ($\mathbf{R} = 0.94$). In contrast, the correlation between the full-section compressive strength of the stub column ($f_{SC} = P_{SC}/A$) with the longitudinal compressive strength obtained from coupon testing ($f_{x,c}$) demonstrates low dependency ($\mathbf{R} = 0.50$).

(iii) The ultimate stub column load ($P_{SC}$) exhibits a more pronounced linear dependency with geometrical parameters than the full-section compressive strength of the stub column ($f_{SC}$).

(iv) The in-plane longitudinal compressive strength associated with the coupon test ($f_{x,c}$) demonstrates **R** values of 0.46 and 0.50 with the ultimate stub column load ($P_{SC}$) and the full-section compressive strength of the stub column ($f_{SC}$), respectively.

(v) Surprisingly, the full-section compressive strength of the stub column ($f_{SC}$) shows a more significant linear dependency with other strength properties derived from coupon tests, particularly with the apparent interlaminar shear strength ($f_{zx}$), the in-plane shear strength ($f_{xy}$), and the transversal compressive strength ($f_{yc}$), with **R** of 0.76, 0.68, and 0.61, respectively.

(vi) The results from Fig. 15 and Fig. 16 show several expected significant correlations, namely between the cross-sectional area and various geometrical parameters ($B$, $H$, $t_B$, and $t_H$), and between the transverse compressive elastic modulus ($E_{y,c}$) and the transverse compressive strength ($f_{y,c}$). Additionally, most matrix-dependent strength properties, including $f_{zx}$, $f_{yc}$, and $f_{xy}$, exhibit strong correlations with each other ($0.86 < \mathbf{R} < 0.90$). On the other hand, such strong correlations are not observed between these strength properties (*i.e.*, $f_{zx}$, $f_{yc}$, and $f_{xy}$) and the shear modulus ($G_{xy}$), or between the longitudinal compressive elastic modulus ($E_{x,c}$) and the longitudinal compressive strength ($f_{x,c}$). Future studies incorporating additional test data should explore these correlations further, thereby providing valuable information for reliability studies and design proposals.

The correlation analysis reveals that shear failure seems to play a significant role in the crushing failure of pGFRP stub columns, which aligns with findings by previous authors [3–5,13]. Although earlier studies examined composite laminates in various applications, they consistently noted the relevance of shear failure for the compressive resistance. This influence of shear failure on the compressive resistance of composites stems from the interaction between complex shear and extensional strain fields. Additionally, the analysis of the failure modes corroborates this interpretation, as "multiple failure modes" were identified, including interfacial, interlaminar, and shear failure types.

While stub columns exhibit a notable correlation with shear strength (namely, $f_{zx}$ and $f_{xy}$), the in-plane compressive strength determined by the CLC method may also be influenced by shear failure modes. According to Bai and Keller [5], this influence becomes more significant when the CLC specimen displays higher geometrical imperfections and a lower ratio of interlaminar shear to compressive strengths. However, CLC coupon specimens are typically free of the main imperfections found in full-scale structures, such as material heterogeneity at junctions and free-end extremities, geometric imperfections along the full-section, residual stresses, and non-uniform fibre distribution. Consequently, the interaction of extensional and shear failures may not be so relevant in CLC coupon tests. In contrast, at the full-section level, where more imperfections exist (both material and geometrical), it is likely that more complex failure occurs, combining shear and extensional failure modes.

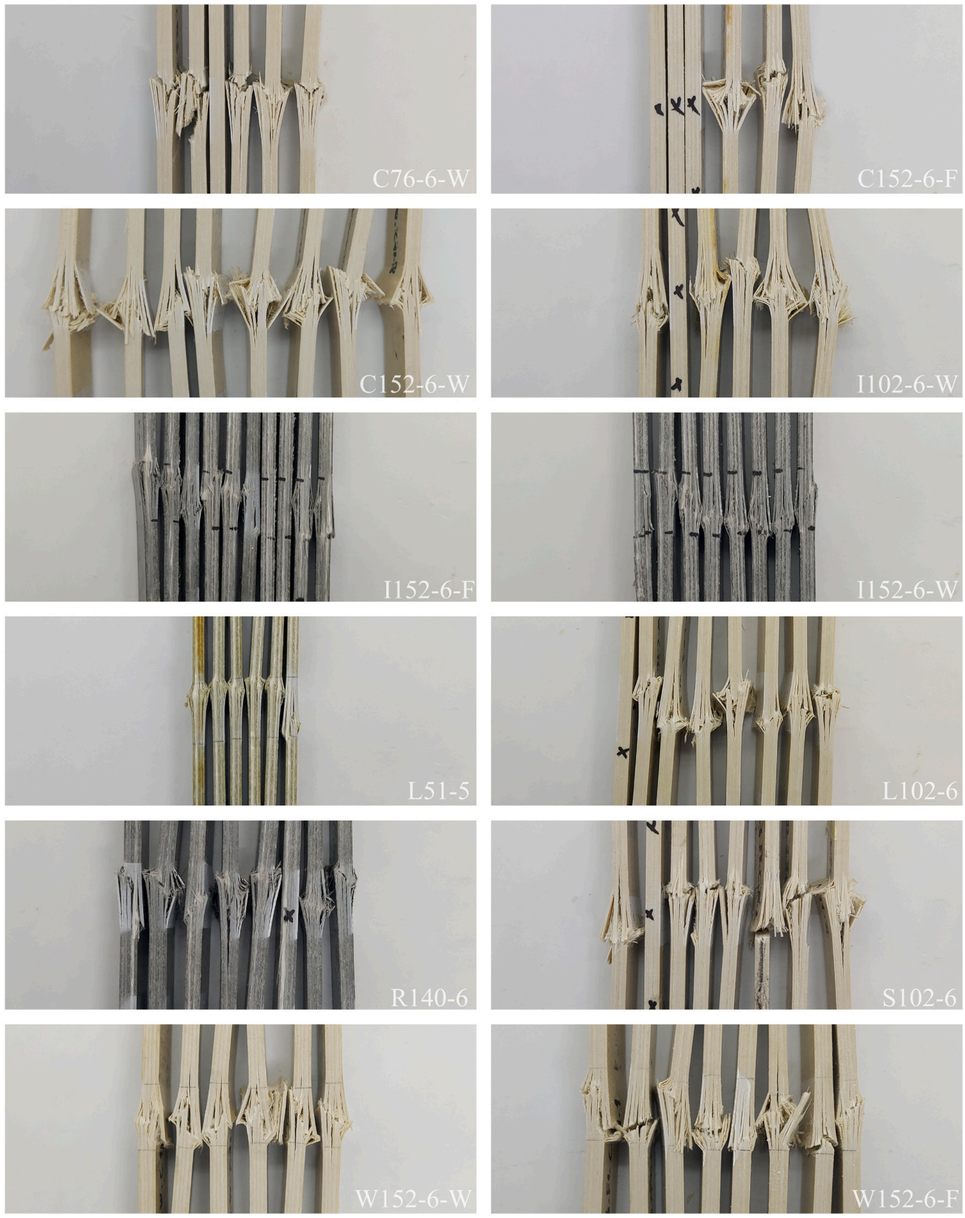


**Fig. 13.** Longitudinal compressive failure of all coupon tests performed according with the CLC method (EN ISO 14126–2001 [15]).

Another potential factor contributing to failure dependency could be the out-of-plane tensile strength and interlaminar shear strength in the *y-z* plane, primarily induced by Poisson strains in the through-thickness direction. While there is no direct mention of the Poisson effect in the compressive failure mode of composites, this hypothesis remains plausible. However, further analysis is necessary to confirm this assumption, involving both experimental and computational methods [54]. For example, experimental tests on the out-of-plane direction [55] and more precise experimental methods for determining the interlaminar strength (such as V-notched Iosipescu tests [33] or shear tests by compression loading of double-notched specimens [56]) could provide further insights. It is worth noting that the current standard for determining the interlaminar shear strength [34], involving a short-beam test, only provides an apparent strength estimate, which may not accurately represent the actual interlaminar shear strength.

## 4. Conclusions

The study outlined in this paper aimed at investigating the material crushing behaviour of full-section pultruded GFRP (pGFRP) stub columns. Extensive experimental data were obtained, including detailed coupon test results for various cross-section shapes. The outcomes indicate that the resistances predicted from standardized small-scale coupon tests are considerably higher than the compressive strength obtained from full-section stub column tests, confirming previous findings. The following main conclusions were drawn:

(i) In terms of axial load/stress *vs*. strain behaviour, the full-section tests revealed a clear linear behaviour with a distinct non-linear effect during the initial stage. This effect may be attributed to factors such as profile-machine alignment, material heterogeneity, or surface flatness irregularities (specimen and/or steel base plates), despite the careful preparation of test specimens and setup. Additionally, there was a noticeable variation in axial strains across the cross-section width, with a clear trend of decreasing “local” compressive modulus estimates from the middle of the web to the flanges.

**Table 8**
CLC coupon tests failure mode classifications according to ASTM D6641-14 and Opelt et al. [13].

| Profile label | ASTM D6641-14 | Opelt et al. (2018) | |
|---|---|---|---|
| | *Failure mode* | *Failure type* | *Failure mode* |
| C76–6 | Multi-mode (end-crushing, through-thickness, delamination) | Interlaminar, shear | Wedge splitting, longitudinal cracking |
| C152–6 | Multi-mode (brooming, end-crushing, through-thickness, delamination) | Shear | Wedge splitting |
| I102–6 | Multi-mode (brooming, end-crushing, through-thickness, delamination) | Interlaminar, shear | Wedge splitting, longitudinal cracking |
| I152–6 | Multi-mode (end-crushing, through-thickness, delamination) | Interlaminar | Delamination buckling |
| L51–5 | Multi-mode (end-crushing, through-thickness, delamination) | Interlaminar | Delamination buckling |
| L102–6 | Multi-mode (end-crushing, through-thickness, delamination) | Shear | Wedge splitting |
| R140–6 | Multi-mode (end-crushing, through-thickness, delamination) | Shear | Through-the-thickness shear |
| S102–6 | Multi-mode (end-crushing, through-thickness, delamination) | Shear | Through-the-thickness shear, wedge splitting |
| W152–6 | Multi-mode (end-crushing, through-thickness, delamination) | Interlaminar, shear | Through-the-thickness shear, wedge splitting, longitudinal cracking |

(ii) Regarding the relative slenderness parametric study of stub columns, several noteworthy observations can be made regarding the accurate determination of the experimental full-section compressive strength. Firstly, some of the recommendations outlined in the ISO 23930 [14] standard (a similar procedure is provided in Annex B of GB/T 31539 [39]) appear inadequate for assessing the compressive strength of stub columns. Alternatively, a more appropriate approach for estimating the "true" slenderness and capturing the pure material crushing behaviour of the full section involves adopting a similar procedure to that proposed by Cardoso et al. [40]. This revised slenderness criterion conservatively limits both plate and member slenderness to a maximum value of 0.7. This refined slenderness approach takes into consideration the occurrence of pure material crushing failure (strength estimates obtained from coupon tests), while accounting for the pure elastic buckling phenomenon.

(iii) Concerning the study involving several cross-sections, the ultimate load determined in the stub column tests was approximately 60 % (on average) of the estimates obtained from coupon tests. This relative difference should be appropriately taken into account in design. The failure mode of the stub columns exhibited an irregular fracture propagation across the in-plane direction ("multiple failure modes"), while in the coupon tests the failure mode presented a uniform fracture across the in-plane direction. The differences in failure modes at the two scales may explain why the results of compressive tests on CLC coupon laminates extracted from the walls of pGFRP profiles do not allow to adequately estimate their full-section crushing resistance.

(iv) The correlation analysis presented in the final part of the paper provided insights about the correlations between different experimental parameters (geometrical and mechanical) that were gathered. The correlation coefficient between the full-section compressive strength and the in-plane longitudinal compressive strength derived from CLC coupon tests was relatively low, approximately 0.50. Surprisingly, the full-section compressive strength of the pGFRP stub columns exhibited a more significant linear dependency with other laminate strengths derived from coupon tests, particularly with the apparent interlaminar shear strength, the in-plane shear strength, and the transversal compressive strength (0.76, 0.68 and 0.61, respectively). This

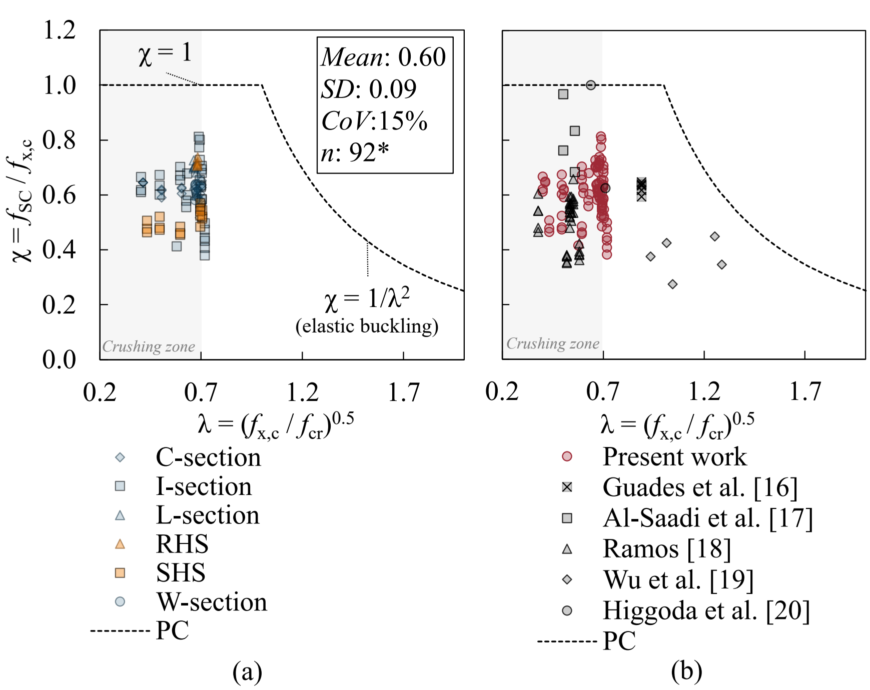


**Fig. 14.** Strength reduction factor ($\chi$) *vs.* relative local slenderness ratio ($\lambda$) of pGFRP stub columns tested compared to the perfect column (PC) curve classified by: (a) cross-section from present work (*specimens C76–6–17, I102–6–31 and S102–6–117 follow ISO 23930 [14] and thus were not considered) and (b) literature data [16–20].

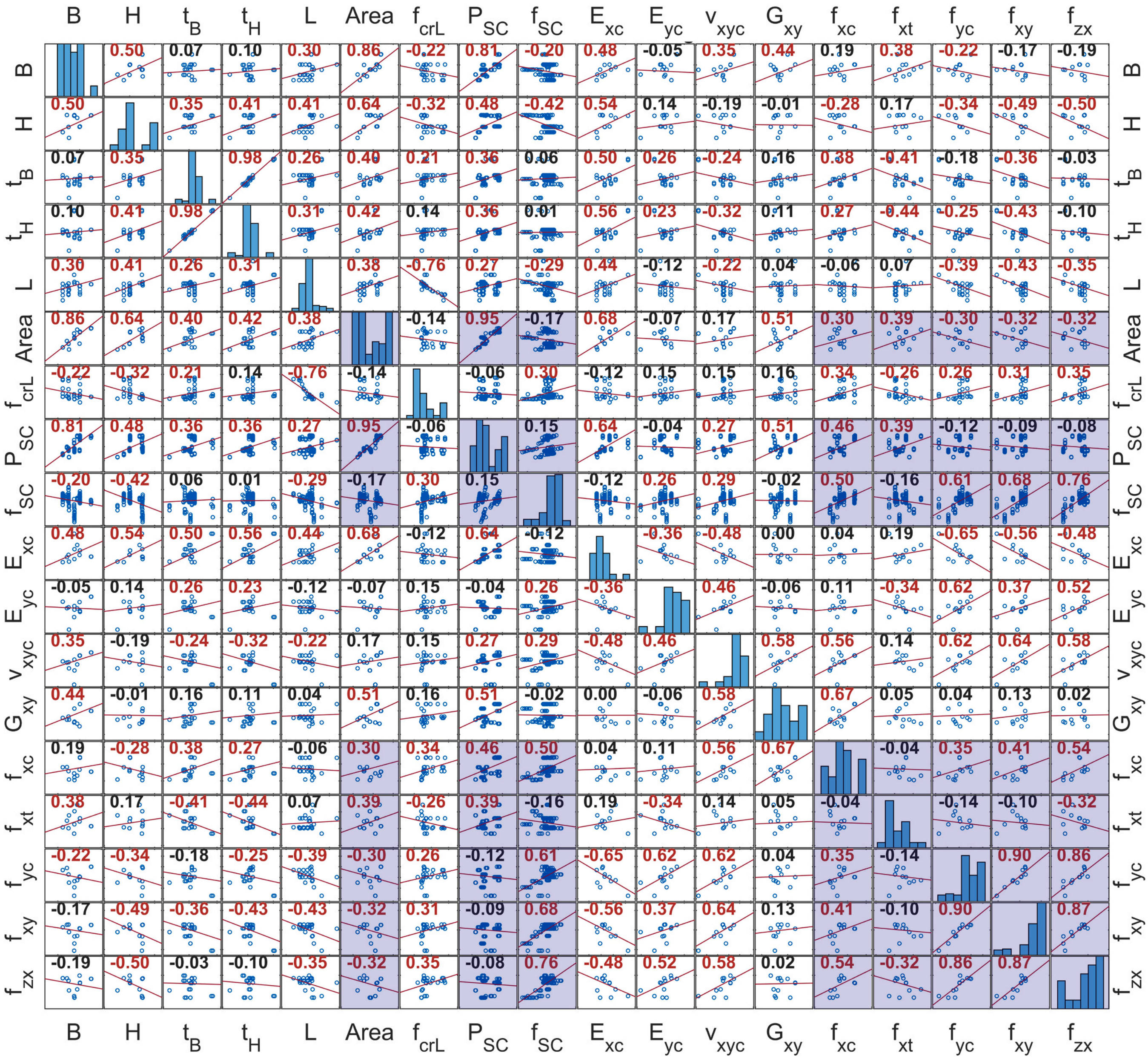


**Fig. 15.** Correlation matrix of experimentally measured geometrical and mechanical properties for stub column and coupon tests performed at the present study (highlighted correlations depicted in Fig. 16).

seems to reflect the fact that the stub column tests encompass a blend of various failure modes. This is supported by the failure mode analysis, in which "multiple failure modes" were identified, including interfacial, interlaminar and shear failure types.

(v) Finally, the results show that the formula included in the European Technical Specification CEN/TS 19101:2022 [9], based solely on the compressive resistance of the CLC coupon tests and cross-sectional area, does not allow to accurately predict the resistance to crushing of pGFRP profiles. Although a strong linear dependency is observed between the experimental ($P_{SC}$) and predicted ($N_{c,R1}$) results, this is mainly due to the strong linear dependency of the cross-sectional area. This suggests that while the cross-sectional area is a dominant factor, the CLC compressive strength from coupon tests does not allow to accurately predict the full-section compressive strength of stub columns, indicating a need for more precise design procedures.

(vi) Overall, stub column tests could be used as a more precise experimental method to determine the compressive resistance of the profiles for design purposes. While CLC coupon testing is a well-established approach for determining the compressive strength at the laminate scale, its results are not accurate for characterizing the full-section compressive resistance of pultruded GFRP profiles.

Future work will focus on computational simulations of the pGFRP stub column tests, considering the progressive failure of the material [31,54], the influence of material heterogeneity along the walls (*e.g.*, resin-rich core at wall junctions), frictional contact between end plates and pGFRP profiles, cut end surfaces flatness and initial geometrical imperfections measured from real scale profiles. Besides computational simulations, future work should focus on gathering data from a wider range of manufacturers, lay-up configurations, fibre and resin types, thicknesses, and geometrical shapes. This will provide deeper insights

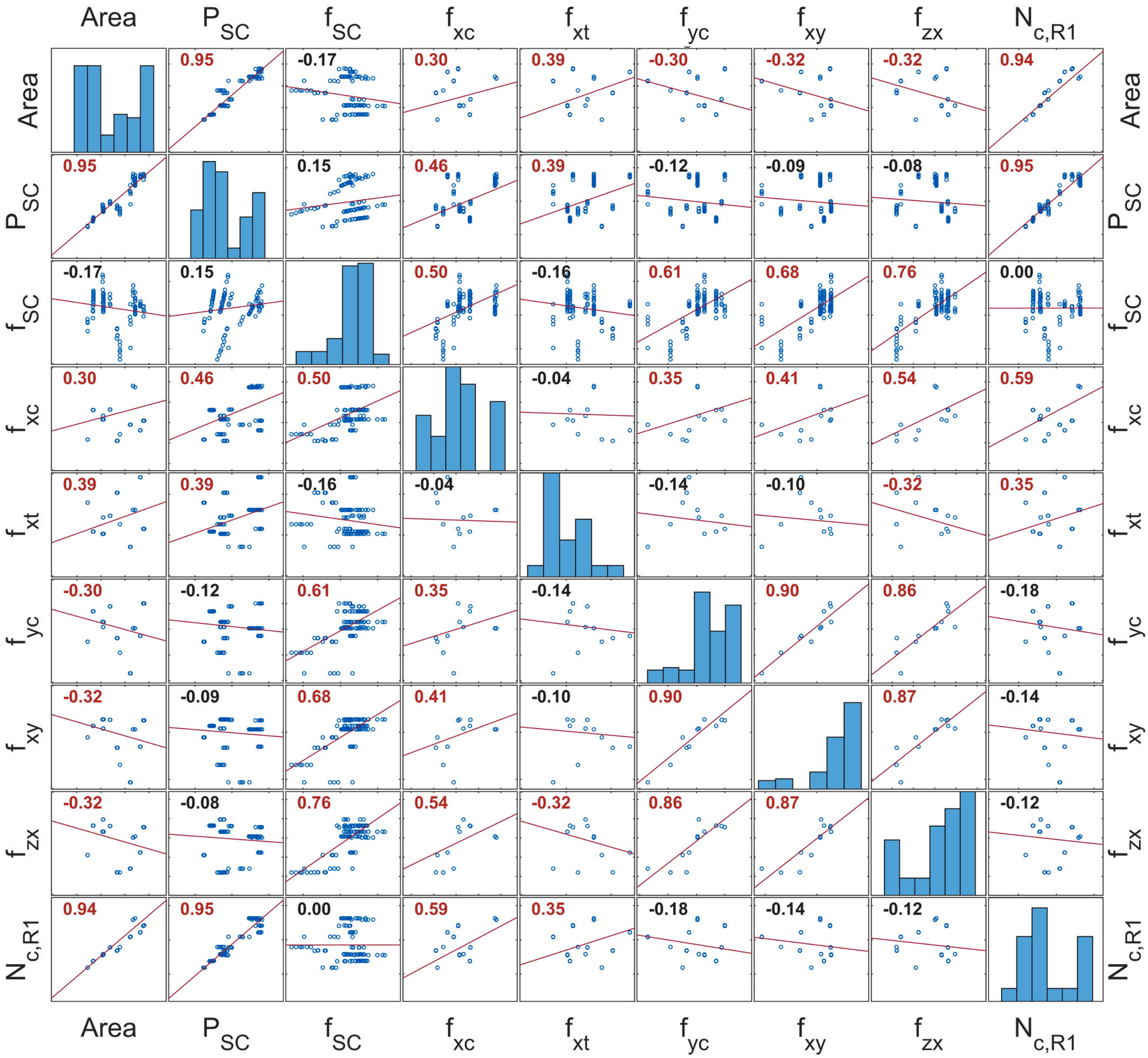


**Fig. 16.** Correlation matrix of key parameters in view of design procedures ($N_{c,R1} = f_{x,c}\,A$, where $A$ is the cross-section area).

and help establish more reliable correlations between geometrical and material properties. In addition, future research will also focus on the statistical variability of geometrical parameters, which directly impacts the uncertainty of design procedures, particularly in slenderness calculations and geometrical properties. Finally, more precise design provisions will be proposed to estimate the full-section resistance to crushing. Partial factors will be calibrated for design purposes and compared with those recommended by international design guidelines [6–10].

## CRediT authorship contribution statement

**João Alfredo de Lazzari:** Writing – original draft, Visualization, Validation, Software, Investigation, Formal analysis, Data curation. **Joao Correia:** Writing – review & editing, Supervision, Resources, Methodology, Funding acquisition, Conceptualization. **José Gonilha:** Writing – review & editing, Supervision, Methodology, Conceptualization. **Nuno Silvestre:** Writing – review & editing, Supervision, Resources, Project administration, Methodology, Funding acquisition.

## Declaration of Generative AI and AI-assisted technologies in the writing process

During the preparation of this work, the first author used OpenAI's tool ChatGPT in order to enhance the language and readability of the first draft. After using this tool/service, the authors reviewed and edited the content as needed and take full responsibility for the content of the publication.

## Declaration of Competing Interest

The authors declare that they have no known competing financial interests or personal relationships that could have appeared to influence the work reported in this paper.

## Data availability

Data will be made available on request.


## Acknowledgements

The authors extend their gratitude to Professors Paulo Martins, João Pedro Pragana, João Magrinho and Beatriz Silva from IDMEC, for providing valuable insights and assistance during the experimental campaign conducted at the Mechanical Testing Laboratory. The first and second authors gratefully acknowledges the financial support given by FCT in the context of the Ph.D. scholarship SFRH/BD/04925/2021 (DOI: 10.54499/2021.04925.BD) and research contract CEECIND/04648/2017/CP1461/CT0015 (DOI: 10.54499/CEECIND/04648/2017/CP1461/CT0015), respectively. All authors gratefully acknowledge the financial support given by FCT to project Reliable-FRP PTDC/ECI-EGC/3916/2021 (DOI: 10.54499/PTDC/ECI-EGC/3916/2021). The authors acknowledge Fundação para a Ciência e a Tecnologia (FCT) for its financial support via the project LAETA Base Funding (DOI: 10.54499/UIDB/50022/2020). This work was supported by FCT, through CERIS (DOI: 10.54499/UIDB/04625/2020).


## Appendix

**Table A.1**
Hardware and software stetting parameters of the DIC system for in-plane strain automatic calculation.

| 2D-DIC System Parameters | Description |
|---|---|
| Camera | Flir® Blackfly model S BFLY-U3–51S5M-C |
| Lens | Fujinon® HF12.5SA−1 F1.4/12.5 mm |
| Lights | Two led lights Dracast® LED500-DV Pro 302 × 158 mm$^2$ |
| Image acquisition frequency | 1 Hz |
| Subset size | 41–45 |
| Step size | 21–23 |
| Correlation criterion Interpolant | Approximated NSSD |
| Correlation subset weight | Uniform |
| Interpolation | Local bicubic spline |
| Shape function | Affine |
| Image pre-filtering | Gaussian with Kernel Size of 5 px |
| Strain window size | 15 |
| Strain tensor | Logarithmic Euler-Almansi |
| Strain interpolation | Improved Quadratic Quadrilateral (Q9) |

**Table A.2**
Crushing data base from experimental results of stub columns.

| Specimen | Shape | $B$ | $H$ | $t_B$ | $t_H$ | $L$ | Area | $P_{cr}$ | $P_{exp}$ |
|---|---|---|---|---|---|---|---|---|---|
| | | (mm) | (mm) | (mm) | (mm) | (mm) | (mm$^2$) | (kN) | (kN) |
| CI6–1 | I-section | 75.8 | 151.8 | 6.1 | 6.2 | 64 | 1787 | 1531 | 375.8 |
| CI6–2 | I-section | 75.8 | 151.8 | 6.1 | 6.2 | 64 | 1787 | 1531 | 395.1 |
| CI6–3 | I-section | 75.8 | 151.8 | 6.1 | 6.2 | 64 | 1787 | 1531 | 322.9 |
| CI6–4 | I-section | 75.8 | 151.8 | 6.1 | 6.2 | 64 | 1787 | 1531 | 343.8 |
| CI6–5 | I-section | 75.8 | 151.8 | 6.1 | 6.2 | 64 | 1787 | 1531 | 351.9 |
| CI6–6 | I-section | 75.8 | 151.8 | 6.1 | 6.2 | 64 | 1787 | 1531 | 300.9 |
| AI8–1 | I-section | 74.7 | 148.9 | 7.6 | 8.0 | 82 | 2208 | 2690 | 648.9 |
| AI8–2 | I-section | 74.8 | 148.9 | 7.7 | 8.1 | 82 | 2230 | 3265 | 451.8 |
| AI8–3 | I-section | 74.8 | 148.9 | 7.7 | 8.1 | 82 | 2230 | 2772 | 632.0 |
| AI8–4 | I-section | 74.8 | 148.9 | 7.7 | 8.1 | 82 | 2232 | 2775 | 608.0 |
| AI8–5 | I-section | 74.7 | 148.8 | 7.7 | 8.0 | 82 | 2218 | 2724 | 737.2 |
| C76–6–17–1* | C-section | 22.1 | 76.3 | 6.4 | 6.4 | 17 | 687 | 2341 | 255.6 |
| C76–6–17–2* | C-section | 22.1 | 76.3 | 6.4 | 6.4 | 17 | 687 | 2341 | 252.9 |
| C76–6–17–3* | C-section | 22.1 | 76.3 | 6.4 | 6.4 | 17 | 687 | 2341 | 246.1 |
| C76–6–30–1 | C-section | 22.1 | 76.3 | 6.4 | 6.4 | 30 | 687 | 2249 | 249.3 |
| C76–6–30–2 | C-section | 22.1 | 76.3 | 6.4 | 6.4 | 30 | 687 | 2249 | 248.7 |
| C76–6–30–3 | C-section | 22.1 | 76.3 | 6.4 | 6.4 | 30 | 687 | 2249 | 249.2 |
| C76–6–40–1 | C-section | 22.1 | 76.3 | 6.4 | 6.4 | 40 | 687 | 1509 | 239.2 |
| C76–6–40–2 | C-section | 22.1 | 76.3 | 6.4 | 6.4 | 40 | 687 | 1509 | 237.8 |
| C76–6–40–3 | C-section | 22.1 | 76.3 | 6.4 | 6.4 | 40 | 687 | 1509 | 227.8 |
| C76–6–49–1 | C-section | 22.1 | 76.3 | 6.4 | 6.4 | 49 | 687 | 1059 | 233.2 |
| C76–6–49–2 | C-section | 22.1 | 76.3 | 6.4 | 6.4 | 49 | 687 | 1059 | 240.9 |
| C76–6–49–3 | C-section | 22.1 | 76.3 | 6.4 | 6.4 | 49 | 687 | 1059 | 241.7 |
| C76–6–59–1 | C-section | 22.1 | 76.3 | 6.4 | 6.4 | 59 | 687 | 779 | 252.0 |
| C76–6–59–2 | C-section | 22.1 | 76.3 | 6.4 | 6.4 | 59 | 687 | 779 | 241.9 |
| C76–6–59–3 | C-section | 22.1 | 76.3 | 6.4 | 6.4 | 59 | 687 | 779 | 245.5 |
| I102–6–31–1* | I-section | 48.8 | 99.4 | 6.0 | 6.0 | 31 | 1109 | 3881 | 357.7 |
| I102–6–31–2* | I-section | 48.8 | 99.4 | 6.0 | 6.0 | 31 | 1109 | 3881 | 365.2 |
| I102–6–31–3* | I-section | 48.8 | 99.4 | 6.0 | 6.0 | 31 | 1109 | 3881 | 358.8 |

(*continued on next page*)

**Table A.2** (*continued*)

| Specimen | Shape | $B$ | $H$ | $t_B$ | $t_H$ | $L$ | Area | $P_{cr}$ | $P_{exp}$ |
|---|---|---|---|---|---|---|---|---|---|
| | | (mm) | (mm) | (mm) | (mm) | (mm) | (mm$^2$) | (kN) | (kN) |
| I102–6–33–1 | I-section | 48.8 | 99.4 | 6.0 | 6.0 | 33 | 1109 | 3525 | 349.0 |
| I102–6–33–2 | I-section | 48.8 | 99.4 | 6.0 | 6.0 | 33 | 1109 | 3525 | 380.7 |
| I102–6–33–3 | I-section | 48.8 | 99.4 | 6.0 | 6.0 | 33 | 1109 | 3525 | 354.0 |
| I102–6–41–1 | I-section | 48.8 | 99.4 | 6.0 | 6.0 | 41 | 1109 | 2332 | 362.9 |
| I102–6–41–2 | I-section | 48.8 | 99.4 | 6.0 | 6.0 | 41 | 1109 | 2332 | 384.7 |
| I102–6–41–3 | I-section | 48.8 | 99.4 | 6.0 | 6.0 | 41 | 1109 | 2332 | 343.6 |
| I102–6–50–1 | I-section | 48.8 | 99.4 | 6.0 | 6.0 | 50 | 1109 | 1609 | 402.0 |
| I102–6–50–2 | I-section | 48.8 | 99.4 | 6.0 | 6.0 | 50 | 1109 | 1609 | 383.3 |
| I102–6–50–3 | I-section | 48.8 | 99.4 | 6.0 | 6.0 | 50 | 1109 | 1609 | 374.5 |
| I102–6–60–1 | I-section | 48.8 | 99.4 | 6.0 | 6.0 | 60 | 1109 | 1159 | 388.9 |
| I102–6–60–2 | I-section | 48.8 | 99.4 | 6.0 | 6.0 | 60 | 1109 | 1159 | 396.7 |
| I102–6–60–3 | I-section | 48.8 | 99.4 | 6.0 | 6.0 | 60 | 1109 | 1159 | 404.0 |
| S102–6–117–1* | SHS | 101.6 | 101.6 | 6.4 | 6.4 | 117 | 2419 | 1000 | 742.6 |
| S102–6–117–2* | SHS | 101.6 | 101.6 | 6.4 | 6.4 | 117 | 2419 | 1000 | 730.9 |
| S102–6–117–3* | SHS | 101.6 | 101.6 | 6.4 | 6.4 | 117 | 2419 | 1000 | 736.4 |
| S102–6–32–1 | SHS | 101.6 | 101.6 | 6.4 | 6.4 | 32 | 2419 | 8673 | 777.8 |
| S102–6–32–2 | SHS | 101.6 | 101.6 | 6.4 | 6.4 | 32 | 2419 | 8673 | 824.6 |
| S102–6–32–3 | SHS | 101.6 | 101.6 | 6.4 | 6.4 | 32 | 2419 | 8673 | 757.2 |
| S102–6–37–1 | SHS | 101.6 | 101.6 | 6.4 | 6.4 | 37 | 2419 | 6631 | 783.3 |
| S102–6–37–2 | SHS | 101.6 | 101.6 | 6.4 | 6.4 | 37 | 2419 | 6631 | 771.8 |
| S102–6–37–3 | SHS | 101.6 | 101.6 | 6.4 | 6.4 | 37 | 2419 | 6631 | 850.9 |
| S102–6–45–1 | SHS | 101.6 | 101.6 | 6.4 | 6.4 | 45 | 2419 | 4583 | 742.6 |
| S102–6–45–2 | SHS | 101.6 | 101.6 | 6.4 | 6.4 | 45 | 2419 | 4583 | 789.5 |
| S102–6–45–3 | SHS | 101.6 | 101.6 | 6.4 | 6.4 | 45 | 2419 | 4583 | 751.4 |
| S102–6–54–1 | SHS | 101.6 | 101.6 | 6.4 | 6.4 | 54 | 2419 | 3282 | 836.3 |
| S102–6–54–2 | SHS | 101.6 | 101.6 | 6.4 | 6.4 | 54 | 2419 | 3282 | 848.0 |
| S102–6–54–3 | SHS | 101.6 | 101.6 | 6.4 | 6.4 | 54 | 2419 | 3282 | 889.0 |
| C76–6-SC–59–1 | C-section | 22.4 | 76.2 | 6.2 | 6.1 | 59 | 670 | 779 | 218.5 |
| C76–6-SC–59–2 | C-section | 22.4 | 76.2 | 6.2 | 6.2 | 59 | 671 | 779 | 210.5 |
| C76–6-SC–59–3 | C-section | 22.3 | 76.2 | 6.2 | 6.2 | 59 | 668 | 779 | 194.4 |
| C76–6-SC–59–4 | C-section | 22.4 | 76.1 | 6.2 | 6.2 | 59 | 671 | 779 | 208.6 |
| C76–6-SC–59–5 | C-section | 22.4 | 76.2 | 6.2 | 6.2 | 59 | 671 | 779 | 228.4 |
| C152–6-SC–55–1 | C-section | 41.4 | 152.0 | 6.2 | 6.3 | 55 | 1387 | 1664 | 457.9 |
| C152–6-SC–55–2 | C-section | 41.4 | 152.0 | 6.2 | 6.2 | 55 | 1375 | 1664 | 482.3 |
| C152–6-SC–55–3 | C-section | 41.5 | 151.8 | 6.2 | 6.2 | 55 | 1373 | 1664 | 458.9 |
| C152–6-SC–55–4 | C-section | 41.4 | 152.2 | 6.2 | 6.2 | 55 | 1375 | 1664 | 499.0 |
| C152–6-SC–55–5 | C-section | 41.4 | 152.0 | 6.2 | 6.2 | 55 | 1374 | 1664 | 480.5 |
| I102–6-SC–60–1 | I-section | 48.9 | 99.1 | 5.7 | 6.0 | 60 | 1081 | 1159 | 446.4 |
| I102–6-SC–60–2 | I-section | 49.0 | 99.1 | 5.6 | 5.9 | 60 | 1068 | 1159 | 447.5 |
| I102–6-SC–60–3 | I-section | 48.9 | 99.0 | 5.7 | 5.9 | 60 | 1071 | 1159 | 427.3 |
| I102–6-SC–60–4 | I-section | 48.9 | 99.1 | 5.7 | 6.0 | 60 | 1079 | 1159 | 404.6 |
| I102–6-SC–60–5 | I-section | 48.9 | 99.1 | 5.7 | 6.0 | 60 | 1078 | 1159 | 363.7 |
| I152–6-SC–60–1 | I-section | 76.2 | 150.5 | 5.7 | 5.7 | 60 | 1662 | 1397 | 383.0 |
| I152–6-SC–60–2 | I-section | 76.2 | 150.5 | 5.8 | 5.8 | 60 | 1689 | 1397 | 405.6 |
| I152–6-SC–60–3 | I-section | 76.3 | 150.2 | 5.7 | 5.8 | 60 | 1667 | 1397 | 429.7 |
| I152–6-SC–60–4 | I-section | 76.2 | 150.4 | 5.7 | 5.8 | 60 | 1674 | 1397 | 435.9 |
| I152–6-SC–60–5 | I-section | 76.3 | 150.3 | 5.7 | 5.8 | 60 | 1682 | 1397 | 401.8 |
| L51–5-SC–44–1 | L-section | 51.0 | 51.1 | 4.6 | 4.6 | 44 | 451 | 402 | 113.7 |
| L51–5-SC–44–2 | L-section | 50.9 | 51.0 | 4.6 | 4.6 | 44 | 448 | 402 | 125.2 |
| L51–5-SC–44–3 | L-section | 51.0 | 51.0 | 4.6 | 4.6 | 44 | 446 | 402 | 124.6 |
| L51–5-SC–44–4 | L-section | 51.0 | 50.9 | 4.6 | 4.6 | 44 | 445 | 402 | 128.3 |
| L51–5-SC–44–5 | L-section | 51.0 | 51.0 | 4.6 | 4.6 | 44 | 447 | 402 | 123.9 |
| L102–6-SC–53–1 | L-section | 99.7 | 99.5 | 5.6 | 5.7 | 53 | 1090 | 1232 | 342.7 |
| L102–6-SC–53–2 | L-section | 99.6 | 99.7 | 5.7 | 5.6 | 53 | 1095 | 1232 | 350.3 |
| L102–6-SC–53–3 | L-section | 99.6 | 99.6 | 5.7 | 5.6 | 53 | 1090 | 1232 | 394.8 |
| L102–6-SC–53–4 | L-section | 99.7 | 99.6 | 5.6 | 5.7 | 53 | 1096 | 1232 | 338.8 |
| L102–6-SC–53–5 | L-section | 99.7 | 99.6 | 5.7 | 5.7 | 53 | 1096 | 1232 | 386.9 |
| R140–6-SC–61–1 | RHS | 88.8 | 139.4 | 6.0 | 6.2 | 61 | 2638 | 2617 | 865.0 |
| R140–6-SC–61–2 | RHS | 88.9 | 139.6 | 6.1 | 6.1 | 61 | 2638 | 2617 | 880.9 |
| R140–6-SC–61–3 | RHS | 88.9 | 139.6 | 6.0 | 6.2 | 61 | 2644 | 2617 | 900.4 |
| R140–6-SC–61–4 | RHS | 88.8 | 139.6 | 6.1 | 6.1 | 61 | 2636 | 2617 | 871.1 |
| R140–6-SC–61–5 | RHS | 88.8 | 139.5 | 6.1 | 6.1 | 61 | 2629 | 2617 | 857.1 |
| S102–6-SC–54–1 | SHS | 101.4 | 101.3 | 6.2 | 6.1 | 54 | 2342 | 3282 | 907.7 |
| S102–6-SC–54–2 | SHS | 101.3 | 101.3 | 6.1 | 6.1 | 54 | 2332 | 3282 | 872.3 |
| S102–6-SC–54–3 | SHS | 101.3 | 101.3 | 6.2 | 6.1 | 54 | 2335 | 3282 | 858.9 |
| S102–6-SC–54–4 | SHS | 101.4 | 101.3 | 6.2 | 6.1 | 54 | 2339 | 3282 | 835.8 |
| S102–6-SC–54–5 | SHS | 101.4 | 101.3 | 6.2 | 6.1 | 54 | 2341 | 3282 | 771.3 |
| W152–6-SC–58–1 | W-section | 152.3 | 150.2 | 6.2 | 6.4 | 58 | 2759 | 3128 | 893.4 |
| W152–6-SC–58–2 | W-section | 152.3 | 150.5 | 6.2 | 6.4 | 58 | 2776 | 3128 | 905.1 |
| W152–6-SC–58–3 | W-section | 153.8 | 150.6 | 6.2 | 6.4 | 58 | 2799 | 3128 | 869.7 |
| W152–6-SC–58–4 | W-section | 152.3 | 150.5 | 6.2 | 6.4 | 58 | 2769 | 3128 | 820.1 |
| W152–6-SC–58–5 | W-section | 152.3 | 150.7 | 6.2 | 6.4 | 58 | 2777 | 3128 | 876.1 |

* Longitudinal length according to ISO 23930:2023, $L = 3r$ (where $r$ is the minor radius of gyration) and $L < 5t$ (for walls with free edges, when it is possible, due to limitation of the profile dimension).

## References


[1] J.R. Correia, Pultrusion of advanced composites, in: J. Bai (Ed.), Advanced Fiber-Reinforced Polymer(FRP) Composites for Structural Applications, second ed., Woodhead Publishing, Elsevier, 2023, pp. 137–177, https://doi.org/10.1016/B978-0-12-820346-0.00007-1.

[2] L.C. Bank, Composites for Construction: Structural Design with FRP Materials, Wiley, New Jersey, 2006, https://doi.org/10.1002/9780470121429.

[3] B.W. Rosen, Mechanics of composite strengthening, in: Fiber Composite Seminar of the American Society for Metals, 1965: pp. 37–75. https://ntrs.nasa.gov/citations/19660035520. (Accessed 27 January 2024).

[4] P.K. Mallick. Fiber-Reinforced Composites, third ed., CRC Press, 2007 https://doi.org/10.1201/9781420005981.

[5] Y. Bai, T. Keller, Shear failure of pultruded fiber-reinforced polymer composites under axial compression, J. Compos. Constr. 13 (2009) 234–242, https://doi.org/10.1061/(ASCE)CC.1943-5614.0000003.

[6] Italian National Research Council, CNR-DT 205/2007 - Guide for the Design and Construction of Structures Made of FRP Pultruded Elements, 2008.

[7] CROW-CUR, Recommendation 96:2019 - Fibre Reinforced Polymers in Buildings & Civil Engineering Structures – Recommendation 96:2019, Gouda, The Netherlands, 2019.

[8] Standard of China Engineering Construction Standardization Association, T/CECS 692-2020 - Technical Specification for Structure of Pultruded Fiber Reinforced Polymer Composites (in Chinese), China Construction Industry, Beijing, China, 2020.

[9] European Committee for Standardization, CEN/TS 19101:2022 - Design of Fibre-Polymer Composite Structures, Technical Committee CEN/TC 250, Brussels, Belgium, 2022.

[10] American Society of Civil Engineers and Structural Engineering Institute, ASCE/SEI 74-23 - Load and Resistance Factor Design (LRFD) for Pultruded Fiber Reinforced Polymer (FRP) Structures, (2024) 1–110. https://doi.org/10.1061/9780784415771.

[11] N. Fleck, Compressive failure of fibre composites, in: J.W. Hutchinson, T.Y. Wu (Eds.), Advances in Applied Mechanics, Academic Press, 1997, pp. 43–119, http://www-mech.eng.cam.ac.uk/profiles/fleck/papers/80.pdf (accessed January 27, 2024).

[12] American Society for Testing and Materials, D6641/D6641M-14: Standard Test Method for Compressive Properties of Polymer Matrix Composite Materials Using a Combined Loading Compression (CLC) Test Fixture, 2014. https://doi.org/10.1520/D6641_D6641M-14.

[13] C.V. Opelt, G.M. Cândido, M.C. Rezende, Compressive failure of fiber reinforced polymer composites – A fractographic study of the compression failure modes, Mater. Today Commun. 15 (2018) 218–227, https://doi.org/10.1016/j.mtcomm.2018.03.012.

[14] International Organization for Standardization, ISO 23930 - Fibre Reinforced Plastic Composites – Full Section Compression Test for Pultruded Profiles, Geneva, Switzerland, 2023. https://www.iso.org/standard/77390.html. (Accessed 9 May 2023)

[15] European Standard, EN ISO 14126:2001 - Fibre-Reinforced Plastic Composites — Determination of Compressive Properties in the In-Plane Direction (version in Spanish), Bruxelles, 2001. https://www.iso.org/standard/23638.html. (Accessed 30 July 2022)

[16] E. Guades, T. Aravinthan, M.M. Islam, Characterisation of the mechanical properties of pultruded fibre-reinforced polymer tube, Mater. Des. 63 (2014) 305–315, https://doi.org/10.1016/j.matdes.2014.06.018.

[17] A.U. Al-Saadi, T. Aravinthan, W. Lokuge, Effects of fibre orientation and layup on the mechanical properties of the pultruded glass fibre reinforced polymer tubes, Eng. Struct. 198 (2019) 109448, https://doi.org/10.1016/j.engstruct.2019.109448.

[18] J.C. Ramos, Compressive Resistance of Pultruded GFRP Profiles, Master Dissertation in Civil Engineering (in Portuguese), Instituto Superior Técnico, University of Lisbon, 2020.

[19] C. Wu, J. Tian, Y. Ding, P. Feng, Axial compression behavior of pultruded GFRP channel sections, Compos Struct. 289 (2022) 115438, https://doi.org/10.1016/j.compstruct.2022.115438.

[20] T.M. Higgoda, M. Elchalakani, M. Kimiaei, A. Wittek, B. Yang, Experimental and numerical investigation of pultruded GFRP circular hollow tubular columns under concentric and eccentric loading, Compos Struct. 304 (2023) 116427, https://doi.org/10.1016/j.compstruct.2022.116427.

[21] American Society for Testing and Materials, ASTM D695-15 - Standard Test Method for Compressive Properties of Rigid Plastics, 2015. https://doi.org/10.1520/D0695-15

[22] P.M.H. Wong, J.M. Davies, Y.C. Wang, An experimental and numerical study of the behaviour of glass fibre reinforced plastics (GRP) short columns at elevated temperatures, Compos Struct. 63 (2004) 33–43, https://doi.org/10.1016/S0263-8223(03)00122-3.

[23] Y. Bai, T. Keller, Modeling of strength degradation for fiber-reinforced polymer composites in fire, J. Compos Mater. 43 (2009) 2371–2385, https://doi.org/10.1177/0021998309344642.

[24] J.R. Correia, M.M. Gomes, J.M. Pires, F.A. Branco, Mechanical behaviour of pultruded glass fibre reinforced polymer composites at elevated temperature: experiments and model assessment, Compos Struct. 98 (2013) 303–313, https://doi.org/10.1016/j.compstruct.2012.10.051.

[25] S. Russo, B. Ghadimi, K. Lawania, M. Rosano, Residual strength testing in pultruded FRP material under a variety of temperature cycles and values, Compos Struct. 133 (2015) 458–475, https://doi.org/10.1016/j.compstruct.2015.07.034.

[26] M.H. Khaneghahi, E.P. Najafabadi, M. Bazli, A. Vatani Oskouei, X.-L. Zhao, The effect of elevated temperatures on the compressive section capacity of pultruded GFRP profiles, Constr. Build. Mater. 249 (2020) 118725, https://doi.org/10.1016/j.conbuildmat.2020.118725.

[27] Creative Composites Group, Creative Composites Group All Categories Catalogue, (2022). https://catalog.creativecompositesgroup.com/viewitems/all-categories. (Accessed 18 July 2022).

[28] Strongwell, EXTREN® Fiberglass Structural Shapes and Plate, (2020). https://www.strongwell.com/products/structural-shapes-and-plate/. (Accessed 23 July 2022)

[29] ALTO Perfis Pultrudidos Lda, Produtos Standard - Perfis reforçados com fibra de vidro (online catalog), (2024). https://alto.pt/perfis_pultrudidos/. (Accessed 25 February 2024)

[30] L. Almeida-Fernandes, N. Silvestre, J.R. Correia, M. Arruda, Compressive transverse fracture behaviour of pultruded GFRP materials: Experimental study and numerical calibration, Compos Struct. 247 (2020), https://doi.org/10.1016/j.compstruct.2020.112453.

[31] J. Gonilha, N. Silvestre, J. R. Correia, V. Tita, D. Martins, Novel progressive failure model for quasi-orthotropic pultruded FRP structures: formulation and calibration of parameters (Part I), Compos Struct. 255 (2021) 112974, https://doi.org/10.1016/J.COMPSTRUCT.2020.112974.

[32] International Organization for Standardization, ISO-527-4:1997 - Determination of Tensile Properties - Part 4: Test Conditions for Isotropic and Orthotropic Fiber-Reinforced Plastic Composites, Bruxelles, 1997

[33] American Society for Testing and Materials, ASTM D5379/D5379M − 12 - Standard Test Method for Shear Properties of Composite Materials by the V-Notched, 2012. https://doi.org/10.1520/D5379_D5379M-12

[34] International Organization for Standardization, EN ISO 14130:1998 - Fibre-Reinforced Plastic Composites Determination of Apparent Interlaminar Shear Strength by Short-Beam Method, 1998

[35] International Organization for Standardization, ISO 1172:1996 - Textile-Glass-Reinforced Plastics - Prepregs, Moulding Compounds and Laminates - Determination of the Textile-Glass and Mineral-Filler Content - Calcination Methods, 1996.

[36] J.A. de Lazzari, L.L. Martins, Á.S. Ribeiro, A. Pinheiro, J.R. Correia, N. Silvestre, Global and local geometrical imperfections of pultruded GFRP profiles based on a modal approach, Constr. Build. Mater. 412 (2024) 134813, https://doi.org/10.1016/j.conbuildmat.2023.134813.

[37] MatchID, Metrology beyond colors, MatchID Version 2024.1, NV: Ghent, Belgium (2024). https://www.matchid.eu/. (Accessed 10 March 2024)

[38] D.C.T. Cardoso, Compressive Strength of Pultruded Glass-Fiber Reinforced Polymer (GFRP) Columns, PhD Thesis, Federal University of Rio de Janeiro, 2014. https://oasisbr.ibict.br/vufind/Record/BRCRIS_6601d7113f15256977698389e3d59c53. (Accessed 23 May 2023)

[39] National Standard of the People's Republic of China, GB/T 31539-2015E - Pultruded Fibre Reinforced Polymer Composites Structural Profiles (English Translation), China Building Materials Federation (2015)

[40] D. Cardoso, K.A. Harries, E.M. Batista, Compressive strength equation for GFRP square tube columns, Compos B Eng. 59 (2014) 1–11, https://doi.org/10.1016/j.compositesb.2013.10.057.

[41] J.A. Lazzari, E.M. Batista, Finite strip method computer application for buckling analysis of thin-walled structures with arbitrary cross-sections, REM - Int. Eng. J. 74 (2021), https://doi.org/10.1590/0370-44672020740065.

[42] Y.K. Cheung, Finite strip method. Structural Analysis, Pergamon Press, 1976.

[43] G.J. Turvey, W.H. Wittrick, Influence of orthotropy on the stability of some multi-plate structures in compression, Aeron. Q 24 (1973) 1–8, https://doi.org/10.1017/s0001925900006363.

[44] N. Silvestre, D. Camotim, GBT buckling analysis of pultruded FRP lipped channel members, Comput. Struct. 81 (2003) 1889–1904, https://doi.org/10.1016/S0045-7949(03)00209-8.

[45] J.D. Vieira, T. Liu, K.A. Harries, Flexural stability of pultruded glass fibre-reinforced polymer I-sections, Proc. Inst. Civ. Eng. Struct. Build. 171 (2018) 855–866, https://doi.org/10.1680/jstbu.16.00238.

[46] D. Cardoso, K.A. Harries, E.M. Batista, Closed-form equations for compressive local buckling of pultruded thin-walled sections, Thin Walled Struct. 79 (2014) 16–22, https://doi.org/10.1016/j.tws.2014.01.013.

[47] D. Cardoso, K.A. Harries, E.M. Batista, Compressive local buckling of pultruded GFRP I-sections: development and numerical/experimental evaluation of an explicit equation, J. Compos. Constr. 19 (2015) 040140421–0401404212, https://doi.org/10.1061/(ASCE)CC.1943-5614.0000501.

[48] European Standard, EN 13706-2:2002 - Reinforced Plastics Composites — Specifications for Pultruded Profiles — Part 2: Method of Test and General Requirements, 3 (2002)

[49] I. Baran, C.C. Tutum, M.W. Nielsen, J.H. Hattel, Process induced residual stresses and distortions in pultrusion, Compos B Eng. 51 (2013) 148–161, https://doi.org/10.1016/j.compositesb.2013.03.031.

[50] A. Vedernikov, F. Tucci, P. Carlone, S. Gusev, S. Konev, D. Firsov, I. Akhatov, A. Safonov, Effects of pulling speed on structural performance of L-shaped pultruded profiles, Compos Struct. 255 (2021) 112967, https://doi.org/10.1016/j.compstruct.2020.112967.

[51] S. Qi, O. Alajarmeh, M. Alhawamdeh, T. Shelley, P. Schubel, K. Rendle-Short, X. Zeng, Formation of non-uniform fibre distribution and its effect on the flexural performance of pultruded GFRP box beams, Compos Struct. 327 (2024) 117695, https://doi.org/10.1016/j.compstruct.2023.117695.

[52] P. Feng, Y. Wu, T. Liu, Non-uniform fiber-resin distributions of pultruded GFRP profiles, Compos B Eng. 231 (2022) 109543, https://doi.org/10.1016/j.compositesb.2021.109543.
[53] N.S. Trahair, M.A. Bradford, D. Nethercot, L. Gardner. The Behaviour and Design of Steel Structures to EC3, fourth ed., CRC Press, London, 2014 https://doi.org/10.1201/9781315273518.
[54] D. Costa, J. A. Gonilha, N. Silvestre, Calibration and validation of a 3D homogenised model to simulate the damage progression of pultruded GFRP composites, Eng. Fail Anal. 149 (2023) 107261, https://doi.org/10.1016/j.engfailanal.2023.107261.
[55] T. Keller, T. Vallée, Adhesively bonded lap joints from pultruded GFRP profiles. Part II: joint strength prediction, Compos B Eng. 36 (2005) 341–350, https://doi.org/10.1016/j.compositesb.2004.11.002.
[56] American Society for Testing and Materials, ASTM C1292-22 - Standard Test Method for Shear Strength of Continuous Fiber-Reinforced Advanced Ceramics at Ambient Temperatures, 2022. https://doi.org/10.1520/C1292-22.